Diffuse Neutron Scattering
of Ni-Au
at Elevated Temperatures

A dissertation submitted to the
Swiss Federal Institute of Technology Zurich

for the degree of
Doctor of Natural Sciences

presented by
Michael Portmann-Orlowski
Dipl. Phys. ETH (ETH Zurich)
born February 23, 1973
Swiss citizen

accepted on the recommendation of
Prof. Dr. G. Kostorz, examiner
Prof. Dr. H. C. Öttinger, co-examiner
Prof. Dr. B. Schönfeld, co-examiner

2002

Danksagung

Meinem Doktorvater, Herrn Prof. G. Kostorz, danke ich für die Betreuung während meiner Dissertation. Es ist heute nicht selbstverständlich, dass wir jungen Forschenden selbstständig Ideen verwirklichen und unsere Kreativität in einem reichhaltigen Umfeld ausleben dürfen. Für kreative Gespräche bin ich dankbar, da ich dadurch neue Wege in der Physik kennenlernen durfte. Ich wünsche meinem Doktorvater auch ruhige, entspannte Momente im immer hektischeren und fordernden Hochschulumfeld, in denen neue Kraft für neue Taten gewonnen werden können.

Herrn Prof. B. Schönfeld danke ich für die lehrreichen und fruchtbaren Diskussionen, die bei der Interpretation von Messdaten und Literatur entstanden. Ich war immer wieder aufs Neue gefordert, meine Ideen zusammenzufassen und zu konkretisieren, um seine kritischen Fragen beantworten zu können. Für die Einsichten in seine langjährige Arbeit möchte ich mich bedanken.

Besonders möchte ich mich bei Herrn Prof. H. C. Öttinger bedanken, der bereit war, das Korreferat zu übernehmen.

Das Paul Scherrer Institut in Villingen (Schweiz) stellte freundlicherweise Strahlzeit an den thermischen Dreiachsenspektrometern DrüchaL und RITA-II, dem Flugzeitspektrometer FOCUS und der Kleinwinkelstreuanlage SANS-I zur Verfügung. Für die tatkräftige Unterstützung während den Experimenten bedanke ich mich speziell bei Herrn Dr. F. Altorfer, Herrn Dr. S. Janssen und Herrn Dr. J. Kohlbrecher. Ohne ihre Hilfe wären die Experimente nicht zustande gekommen.

Bei Herrn Dr. C. Wolverton bedanke ich mich für die Nahordnungsparameter, die er mittels Elektronenstrukturberechnungen für Ni-60 at.% Au Mischkristalle bestimmt und uns zur Verfügung gestellt hat. Sie waren uns eine grosse Hilfe bei der Diskussion der Nahordnungsstreuung von Ni-60 at.% Au.

Frau U. Huck möchte ich danken für ihre spontane Hilfe in allen Fragen, die ein Doktorandenleben mit sich bringen. Ihre Anwesenheit am Institut hat frischen Wind ins Institut gebracht. Herrn E. Fischer danke ich für seine ansteckende Begeisterung und seinen Optimismus, welche er in die Kristallzucht und die Probenpräparation einbrachte. Aus seiner Fröhlichkeit und Weltoffenheit konnte ich Kraft und Freude gewinnen. Herrn J. Hecht danke ich für die tatkräftige Mithilfe bei den spontanen

Contents

Curriculum vitae   **77**

Summary

In the solid state, the binary system Ni-Au is often considered a prototype of a phase-separating alloy, as the atomic sizes of its constituents largely differ. In earlier investigations of the solid solution Ni-60 at.% Au above the miscibility gap using diffuse X-ray scattering (Wu and Cohen, 1983), short-range order and no precursor of phase separation was found. This unexpected result was supported by electronic structure calculations (Wolverton and coworkers, 1998).

Diffuse neutron scattering of solid solutions provides a quantitative analysis of the local atomic arrangements and the static atomic displacements. In this work, the local atomic arrangements of ^{58}Ni-8.4 at.% Au and ^{58}Ni-60 at.% Au single crystals in the solid solution above the miscibility gap, at 1083 K and 1023 K, were investigated by elastic diffuse neutron scattering. The Ni-58 isotope was used to reduce the incoherent scattering and to improve the coherent scattering contrast. Thermal diffuse scattering was separated experimentally.

In contrast to previous investigations, a tendency towards decomposition was found. This can be unequivocally concluded from an increase in the elastic diffuse scattering near the incident beam, a region in reciprocal space not investigated in previous diffuse X-ray scattering experiments. For larger scattering vectors, the elastic diffuse scattering is mainly due to the displacement scattering resulting from the large difference in the atomic sizes of Ni and Au. For ^{58}Ni-60 at.% Au, only scattering intensities along $\langle 100 \rangle$ were measured, for ^{58}Ni-8.4 at.% Au scattering intensities within a volume in reciprocal space. Thus, for ^{58}Ni-8.4 at.% Au, it was possible to separate short-range order scattering from the linear and quadratic displacement scattering using least-squares fitting, and a set of Warren-Cowley short-range order parameters was determined. The Warren-Cowley short-range order parameter for the shell of nearest neighbors has a positive value, indicating a preference for like atoms in nearest-neighbor shells (i.e. decomposition).

Crystals modeled on the basis of the Warren-Cowley short-range order parameters, show small Au clusters consisting of a tetrahedron and an attached fifth Au atom as a characteristic feature. In a detailed configurational analysis, basic building elements of the $L1_0$ structure were also found. The $L1_0$ structure was suggested as superstructure for a metastable state by Zhao and Notis (1999).

In a first evaluation of the elastic diffuse neutron scattering of ^{58}Ni-8.4 at.% Au at 1083 K, a value of 0.59(3) was found for the short-range order parameter α_{000}, much smaller than the theoretical value of 1. Values smaller than 1 were repeatedly obtained from diffuse neutron scattering experiments performed at elevated temperatures. These values can now be clearly traced back to a reduction of the transmission factor for increasing temperatures. For ^{58}Ni-8.4 at.% Au at 1083 K, the as-measured transmission factor is 22(4)% lower than at room temperature. The reason for the reduction is an increase in thermal diffuse scattering. Using the correct linear absorption coefficient in the evaluation of the diffuse neutron scattering of ^{58}Ni-8.4 at.% Au, a value of 0.99(4) was obtained for α_{000}.

In the small-angle neutron scattering of ^{58}Ni-8.3 at.% Au polycrystals at elevated temperatures, an additional scattering contribution was obtained, that increases linearly with increasing temperature. It was approximately calculated using incoherent and coherent one-phonon scattering. The remaining elastic small-angle neutron scattering smoothly merges with the elastic wide-angle scattering data.

Zusammenfassung

Das binäre System Ni-Au im festen Zustand wird oft als Prototyp eines entmischenden Legierungssystems betrachtet, da dessen Komponenten einen grossen Atomgrössen-unterschied aufweisen. In früheren Untersuchungen der Mischkristallphase von Ni-60 at.% Au durch diffuse Röntgenstreuung (Wu und Cohen, 1983) wurde oberhalb der Mischungslücke Nahordnung und kein Vorläufer für Entmischung gefunden. Dieses unerwartete Ergebnis wurde mittels Elektronenstrukturberechnungen (Wolverton und Mitarbeiter, 1998) bestätigt.

Die diffuse Neutronenstreuung an Mischkristallen gestattet eine quantitative Beschreibung der lokalen atomaren Anordnung und der statischen atomaren Verschiebungen. In der vorliegenden Arbeit wurde die lokale Anordnung der Atome in ^{58}Ni-8,4 at.% Au und ^{58}Ni-60 at.% Au Einkristallen in der Mischkristallphase bei 1083 K bzw. 1023 K mittels elastisch diffuser Neutronenstreuung untersucht. Das Ni-58-Isotop wurde eingesetzt, um die inkohärente Streuung zu reduzieren und den kohärenten Streukontrast zu erhöhen. Es wurde ausgenutzt, dass die thermisch diffuse Streuung experimentell separiert werden kann.

Im Gegensatz zu früheren Untersuchungen wurde eine Tendenz zur Nahentmischung festgestellt. Dies zeigt sich direkt in einem Anstieg der diffusen Streuung nahe am direkten Strahl, einem Bereich im reziproken Raum, der mittels diffuser Röntgenstreuung nicht untersucht worden war. Im Bereich grösserer Streuvektoren ist die Verzerrungsstreuung der dominierende Streubeitrag; er rührt vom grossen Unterschied in den Atomgrössen der Legierungspartner her. Für ^{58}Ni-60 at.% Au wurden Streuintensitäten entlang $\langle 100 \rangle$ gemessen, für ^{58}Ni-8,4 at.% Au in einem Volumen des reziproken Raumes. Für ^{58}Ni-8,4 at.% Au konnte somit mit der Methode der kleinsten Fehlerquadrate die Nahordnungstreuung von der linearen und quadratischen Verzerrungsstreuung separiert und die Warren-Cowley-Nahordnungsparameter bestimmt werden. Der Warren-Cowley-Nahordnungsparameter für die Schale nächster Nachbarn ist positiv, was einer bevorzugten Anordnung von Atomen der gleichen Sorte als nächste Nachbarn entspricht.

Modellkristalle, die mittels der Warren-Cowley-Nahordnungsparameter erzeugt wurden, zeigen als charakteristisches Bauelement kleine Goldagglomerate, bestehend aus einem Tetraeder und einem fünften angehängten Goldatom. In einer detaillierten

Konfigurationsanalyse wurden auch Bauelemente der $L1_0$-Struktur gefunden, die als möglicher metastabiler Zustand von Zhao und Notis (1999) vorgeschlagen worden war.

In einer ersten Auswertung der diffusen Neutronenstreuung von ^{58}Ni-8,4 at.% Au bei 1083 K wurde für den Nahordnungsparameter α_{000} ein Wert von 0,59(3) bestimmt, deutlich kleiner als der theoretische Wert 1. Zu niedrige Werte von α_{000} wurden wiederholt bei Messungen der elastisch diffusen Neutronenstreuung bei hohen Temperaturen erhalten. Diese Werte können jetzt mit der Abnahme des Transmissionsfaktors bei steigender Temperatur erklärt werden. Für ^{58}Ni-8,4 at.% Au bei 1083 K ist der Transmissionsfaktor um 22(4)% kleiner als bei Zimmertemperatur. Grund dafür ist die Zunahme der thermisch diffusen Streuung. Mit korrektem linearen Absorptionskoeffizienten ergibt sich in der Auswertung der diffusen Neutronenstreuung von ^{58}Ni-8,4 at.% Au für α_{000} ein Wert von 0,99(4).

In der Neutronenkleinwinkelstreuung von ^{58}Ni-8,3 at.% Au Polykristallen bei hohen Temperaturen wurde ein zusätzlicher Streubeitrag gefunden, der näherungsweise linear mit der Temperatur ansteigt. Er konnte mit Hilfe der kohärenten und inkohärenten Einphononenstreuung näherungsweise als thermisch diffuse Streuung berechnet werden. Die verbleibende elastische Neutronenkleinwinkelstreuung geht nahezu glatt in die elastisch diffuse Streuung bei grösseren Winkeln über.

1 Introduction

The local atomic arrangement and the species-dependent static atomic displacements from the average lattice in a solid solution characterize its microstructure. Local correlations in the occupation of the lattice sites are referred to as short-range order. These correlations are a direct consequence of the interaction between the constituents. For states in thermal equilibrium, the interatomic interaction can be determined from the short-range order. Well founded methods to determine short-range order quantitatively are based on the diffuse scattering of neutrons and X-rays (e.g. [Kost96], [Scho99a]). They additionally provide information on the static atomic displacements resulting from the difference in the atomic sizes of the constitutents.

In textbooks, Ni-Au is often presented as a prototype for a phase-separating alloy with a large difference in the atomic sizes ($\sim15\%$) of its constituents (cf. Hume-Rothery rule). The condensed equilibrium phases of Ni-Au (see Fig. 1) are the liquid L with a minimum freezing point of ~1228 K at ~42.5 at.% Ni, and the fcc solid solution with a miscibility gap at low temperatures. The critical point of the miscibility gap is at 1083.3 K for ~70.6 at.% Ni. From measurements of the electromotive force in a galvanic cell between 900 and 1183 K (e.g. [Seig52], [Sell66], [Hofe82]), positive values for the enthalpy of mixing were determined, corresponding to a clustering tendency. Thus, one expects that the solid solution above the miscibility gap is characterized by first precursors for phase separation, leading to maxima in the diffuse scattering near the incident beam and at the positions of the fundamental Bragg reflections.

Surprisingly, in most of the diffuse X-ray scattering experiments (e.g. [Flin51], [Flin53], [Wu83]), maxima in the diffuse scattering between the fundamental reflections were found, a feature that is attributed to an ordering tendency. An alloy system showing a tendency for phase separation at low temperatures which corresponds to a positive enthalpy of mixing and exhibiting short-range order at elevated temperatures, offers an attractive problem for electronic structure calculations. Short-range order scattering patterns calculated by Wolverton and Zunger [Wolv97] agree well with the experimental data of Wu and Cohen [Wu83] and also explained the decomposition at low temperatures.
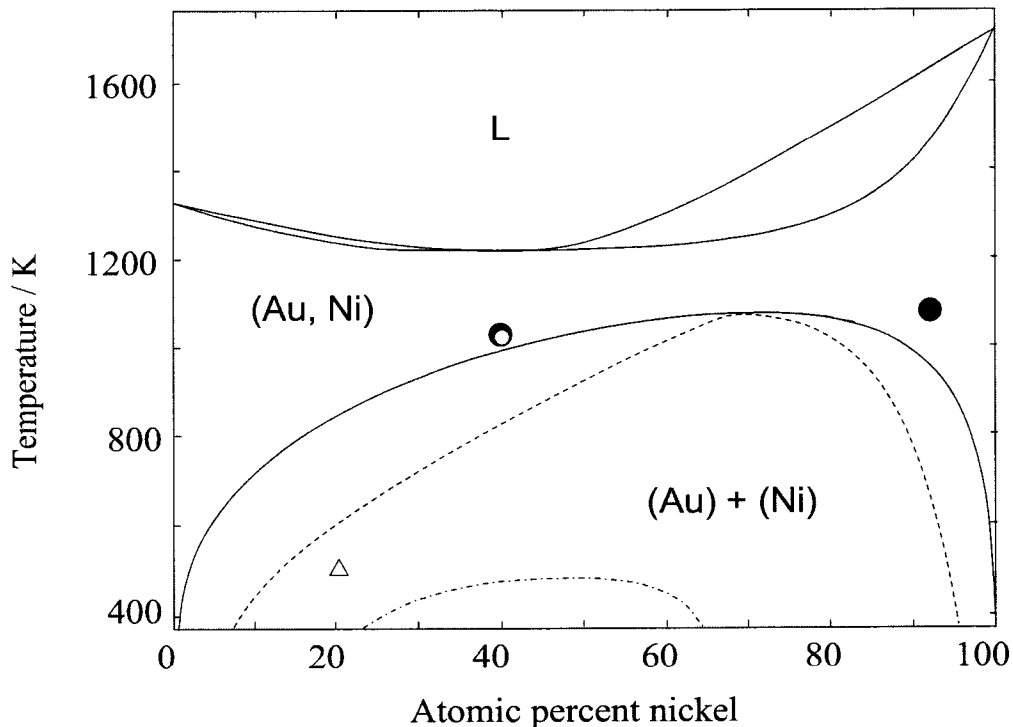
Fig. 1: Phase diagram according to Okamoto [Okam87]. The symbols mark states investigated by Wu and Cohen [Wu83] (o), this work (•) and Renaud and coworkers [Rena95] (△) (condition before aging). The chemical spinodal (dashed line) and the coherent spinodal (dashed-dotted line) [Hofe85] are also shown.

Although the short-range ordered state of the solid solution above the miscibility gap seems to be well established, another experimental proof of this state with present-day experimental tools was called for. In diffuse X-ray scattering experiments, inelastic scattering contributions can not be separated experimentally; they have to be calculated on the basis of elastic constants and subtracted from the total diffuse scattering. Therefore, the diffuse neutron scattering of two Ni-Au alloys was measured in the present work on a triple-axis spectrometer, optimizing the scattering contrast by the use of the Ni-58 isotope instead of natural Ni.

A sensitive parameter to indicate the quality of the separation of the short-range order scattering is the Warren-Cowley short-range order parameter α_{000}. By theory, it has to be 1 (it means that at a given lattice site there is just one atom). In diffuse neutron scattering experiments performed on Fe-rich Fe-Al single crystals at 878, 966 and 1073 K, a systematic decrease (up to 50%) in the value of α_{000} with increasing temperature was found. Since a low value was also found for ^{58}Ni-9.6 at.% Ti [Buch99a] at 1103 K (see Fig. 2), a systematic trend seems to exist. In
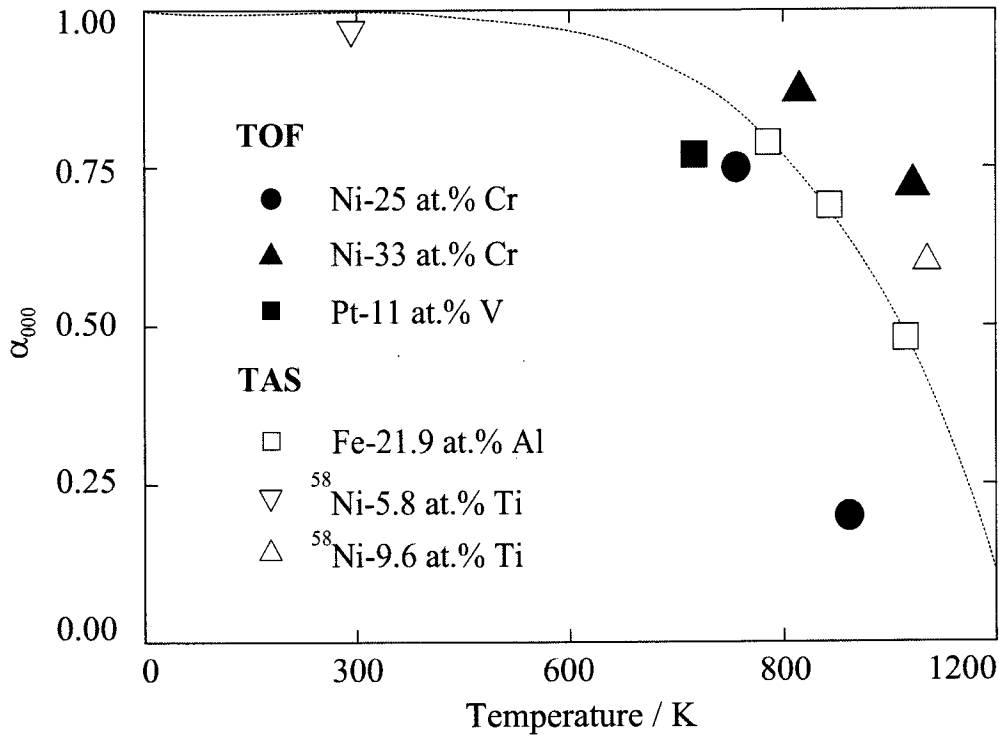
Fig. 2: Values for α_{000} obtained from elastic diffuse neutron scattering using a triple-axis spectrometer (TAS) or a time-of-flight spectrometer (TOF). The dashed line indicates the temperature dependence of the α_{000} value.

experiments using the time-of-flight scattering technique, a less systematic trend was observed (see Table 10 in appendix A). Only for Pt-11 at.% V, Ni-22 at.% Cr and Ni-33 at.% Cr, the value of α_{000} was found to decrease with increasing temperature.

To correct the scattering data (to obtain $\alpha_{000} = 1$), two types of corrections were repeatedly employed; (i) Caudron and coworkers [Caud92] rescaled α_{000} using an additive term, a correction that has no consequences on the short-range order parameters for all neighboring shells. (ii) Le Bolloc'h [Boll97] rescaled the complete set of short-range order parameters, a correction method that changes the values of all short-range order parameters. As the subsequent characterization of the local atomic arrangement is based on the short-range order parameters and therefore could depend on the correction employed, an appropriate correction for α_{000} was searched. The detailed reasons for the unexpected loss in elastic diffuse scattering intensity at elevated temperatures remained unknown. Therefore, the aim of this work was to provide a physical explanation and correction for the expected low value of α_{000} for Ni-8.4 at.% Au, and thus also for the other investigations summarized in Fig. 2.

2 Methods and definitions

2.1 Local atomic arrangements and static atomic displacements

The microstructure of a substitutional solid solution is characterized by the (static) arrangement of the atoms on an average lattice and the species-dependent static atomic displacements due to different atomic sizes. Knowledge of both these features on an atomic scale is of interest for the understanding of macroscopic properties of real crystals.

Local atomic arrangement. The actual arrangement of an A-B alloy on the average lattice is given by the site occupation number $p_{\underline{r}}^{\mu}$ (μ = A,B) where

$$p_{\underline{r}}^{\mu} = \begin{cases} 1 & \text{if site } \underline{r} \text{ is occupied by a } \mu \text{ atom} \\ 0 & \text{otherwise.} \end{cases} \tag{1}$$

Since the occupation of an individual lattice site $\underline{r}$ cannot be determined in an experiment, macroscopic averages over the whole crystal have to be considered. The concentration of the component μ corresponds to the one-point correlation function (brackets denote the configurational average)

$$\langle p_{\underline{r}}^{\mu} \rangle = \frac{1}{N} \sum_{\underline{r}} p_{\underline{r}}^{\mu} = c_{\mu} \tag{2}$$

where N is the total number of atoms in the crystal and $c_{\text{A}} + c_{\text{B}} = 1$. The pair-correlation function

$$\langle p_{\underline{r}}^{\mu} p_{\underline{r}+d\underline{r}}^{\nu} \rangle = \frac{1}{N} \sum_{\underline{r}} p_{\underline{r}}^{\mu} p_{\underline{r}+d\underline{r}}^{\nu} \tag{3}$$

describes the probability to find an atom ν located at $\underline{r}'$ at a fixed distance $|d\underline{r}| = |\underline{r}' - \underline{r}|$ from an atom μ located at $\underline{r}$. For a statistically uncorrelated atomic arrangement, $\langle p_{\underline{r}}^{\mu} p_{\underline{r}+d\underline{r}}^{\nu} \rangle$ corresponds to the product of the concentrations of the ν and μ atoms. General expressions for alloys with more constituents or higher-order correlation functions are given by Inden and Pitsch [Inde91].

The conditional probability $P_{d\underline{r}}^{\mu\nu}$ of finding an atom ν in the neighboring shell

(defined by the fixed distance $d\underline{r}$) of an atom μ is given by

$$P_{d\underline{r}}^{\mu\nu} = \frac{\langle p_{\underline{r}}^{\mu} p_{\underline{r}+d\underline{r}}^{\nu} \rangle}{c_{\mu}}. \tag{4}$$

Using the statistically uncorrelated arrangement as a reference, pair correlations may be characterized by

$$\alpha_{d\underline{r}}^{\mu\nu} = 1 - \frac{P_{d\underline{r}}^{\mu\nu}}{c_{\nu}}. \tag{5}$$

The $\alpha_{d\underline{r}}^{\mu\nu}$ ($\mu \neq \nu$) are the generalized Warren-Cowley [Cowl50a] short-range order parameters. For binary alloys, μ, $\nu \in (A, B)$, the short-range order parameter is

$$\alpha_{d\underline{r}}^{AB} = 1 - \frac{P_{d\underline{r}}^{AB}}{c_B}. \tag{6}$$

As the probability of finding an atom B at a distance $|d\underline{r}| = 0$ from an atom A is equal to zero, $\alpha_{\underline{0}}$ must be unity. Furthermore, the short-range parameter $\alpha_{d\underline{r}}$ allows the atomic arrangements to be grouped in three categories.

(*i*) For a statistically uncorrelated atomic arrangement, $P_{d\underline{r} \neq \underline{0}}^{AB}$ is equal to c_B for any neighboring shell, and the $\alpha_{d\underline{r} \neq \underline{0}}$ are zero.

(*ii*) For a short-range ordered atomic arrangement, $P_{d\underline{r}}^{AB}$ for the nearest neighbors is larger than c_B, and the value of $\alpha_{d\underline{r}}$ is negative.

(*iii*) For a short-range decomposed atomic arrangement, $P_{d\underline{r}}^{AB}$ for the nearest neighbors is smaller than c_B, and the value of $\alpha_{d\underline{r}}$ is positive.

While $\alpha_{d\underline{r}}$ tends to zero with $|d\underline{r}| \to \infty$ for a short-range ordered state, it will keep non-zero values for a long-range ordered state. If $\alpha_{d\underline{r}}$ for nearest neighbors is small in magnitude, it seems more appropriate to determine the state of order from the position of the global maximum in the short-range order scattering (see comments in [Wolv98]).

Species-dependent static atomic displacements. Owing to the different atomic sizes, the atoms are displaced from the positions of the average lattice, and displacement scattering is observed. Two correlations are used to describe the displacement scattering: (*i*) the displacement-difference-weighted pair correlation and (*ii*) the pair correlation of the displacements. The actual position $\underline{r}$ of an atom is described by

$$\underline{r} = \underline{R} + \underline{\delta}_{\underline{r}} \tag{7}$$

where $\underline{R}$ is the nearby position of the average lattice and $\underline{\delta}_{\underline{r}}$ the displacement from the average lattice. Using the site occupation number $p_{\underline{r}}^{\mu}$, the species-independent displacements $\underline{\delta}_{\underline{r}}$ are converted (mathematically) to species-dependent ones by

$$\underline{\delta}_{\underline{r}}^{\mu} = p_{\underline{r}}^{\mu}\underline{\delta}_{\underline{r}}. \tag{8}$$

The species-dependent static atomic displacements $\underline{\delta}_{d\underline{r}}^{\mu\nu}$ between atoms μ and ν are defined as

$$\underline{\delta}_{d\underline{r}}^{\mu\nu} = \underline{\delta}_{\underline{r}}^{\mu} - \underline{\delta}_{\underline{r}+d\underline{r}}^{\nu}. \tag{9}$$

Since the static atomic displacements can not be determined at an individual site $\underline{r}$ in a scattering experiment, one defines the macroscopic average over the species-dependent static atomic displacements of all pairs of atoms at a fixed average distance $|d\underline{r}|$

$$\langle \underline{\delta}_{d\underline{r}}^{\mu\nu}\rangle = \frac{\sum_{\underline{r}} p_{\underline{r}}^{\mu}p_{\underline{r}+d\underline{r}}^{\nu}\left(\underline{\delta}_{\underline{r}+d\underline{r}} - \underline{\delta}_{\underline{r}}\right)}{\sum_{\underline{r}} p_{\underline{r}}^{\mu}p_{\underline{r}+d\underline{r}}^{\nu}}. \tag{10}$$

Only two of the four vectors $\langle \underline{\delta}_{d\underline{r}}^{\mu\nu}\rangle$ are independent; (i) a change of the type of atoms as central atoms changes the sign of $\langle \underline{\delta}_{d\underline{r}}^{\mu\nu}\rangle$. ($ii$) The sum of all species-dependent static atomic displacements of a given distance $|d\underline{r}|$ is zero since they represent deviations from an average lattice. Thus, the average displacement between an A and a B atom in terms of $\langle \underline{\delta}_{\underline{r}}^{AA}\rangle$ and $\langle \underline{\delta}_{\underline{r}}^{BB}\rangle$ is

$$\langle \underline{\delta}_{d\underline{r}}^{AB}\rangle = -\frac{1}{2}\left(\frac{\alpha_{d\underline{r}} + c_A/c_B}{1 - \alpha_{d\underline{r}}}\langle \underline{\delta}_{d\underline{r}}^{AA}\rangle + \frac{\alpha_{d\underline{r}} + c_B/c_A}{1 - \alpha_{d\underline{r}}}\langle \underline{\delta}_{d\underline{r}}^{BB}\rangle\right) = -\langle \underline{\delta}_{d\underline{r}}^{BA}\rangle, \tag{11}$$

using $\langle \underline{\delta}_{d\underline{r}}^{AA}\rangle$ and $\langle \underline{\delta}_{d\underline{r}}^{BB}\rangle$ as independent variables. These variables are usually given in terms of the unit vectors $\underline{e}_i = \underline{a}_i/|\underline{a}_i|$ of the average lattice ($\underline{a}_i$ are real space lattice vectors)

$$\langle \underline{\delta}_{\underline{r}}^{\mu\mu}\rangle = \langle X_{d\underline{r}}^{\mu\mu}\rangle \underline{e}_1 + \langle Y_{d\underline{r}}^{\mu\mu}\rangle \underline{e}_2 + \langle Z_{d\underline{r}}^{\mu\mu}\rangle \underline{e}_3. \tag{12}$$

Depending on the symmetry of the average lattice for fixed distances $|d\underline{r}|$, the species-dependent static atomic displacements $\langle X_{d\underline{r}}^{\mu\mu}\rangle$, $\langle Y_{d\underline{r}}^{\mu\mu}\rangle$, $\langle Z_{d\underline{r}}^{\mu\mu}\rangle$ might be equal in magnitude or could even be zero.

Pair correlation function of individual displacements. The pair correlation of the static atomic displacement $\underline{\delta}_{\underline{r}}^{\mu}$ of an atom μ with the static atomic displacement $\underline{\delta}_{\underline{r}+d\underline{r}}^{\nu}$ of an atom ν at a fixed average distance $d\underline{r}$ is given by

$$\langle \underline{\delta}_{\underline{r}}^{\mu}\underline{\delta}_{\underline{r}+d\underline{r}}^{\nu}\rangle = \frac{\sum_{\underline{r}} p_{\underline{r}}^{\mu}p_{\underline{r}+d\underline{r}}^{\nu}\left(\underline{\delta}_{\underline{r}}\,\underline{\delta}_{\underline{r}+d\underline{r}}\right)}{\sum_{\underline{r}} p_{\underline{r}}^{\mu}p_{\underline{r}+d\underline{r}}^{\nu}}. \tag{13}$$

For $d\underline{r} = \underline{0}$ the zeroth term of the correlation $\langle \delta_{\underline{r}}^{\mu} \delta_{\underline{r}+d\underline{r}}^{\nu} \rangle$ does not have a zero value, but it has no practical meaning, in contrast to $\alpha_{\underline{0}}$ (contrary to Tibballs [Tibb79]). All correlations $\langle \delta_{\underline{r}}^{\mu} \delta_{\underline{r}+d\underline{r}}^{\nu} \rangle$ are independent variables since

$$\sum_{\mu} \sum_{\nu} \langle p_{\underline{r}}^{\mu} p_{\underline{r}+d\underline{r}}^{\nu} \rangle \langle \delta_{\underline{r}}^{\mu} \delta_{\underline{r}+d\underline{r}}^{\nu} \rangle = \left(\sum_{\underline{r}} \delta_{\underline{r}} \right)^2 \neq 0. \qquad (14)$$

In a scattering experiment, the pair correlations of individual static displacements are again given in terms of unit vectors of the average lattice, e.g. $\langle X_{\underline{r}}^{\mu} Y_{\underline{r}+d\underline{r}}^{\nu} \rangle$.

2.2   Diffuse neutron scattering

The elastic coherent scattering of a crystalline solid solution comes from the average lattice occupied by species-averaged atoms and deviations from the average lattice either due to correlations in the local atomic arrangement on the average lattice or due to the atomic displacements from the average lattice. The average lattice leads to Bragg scattering, while all deviations from the translational invariance result in diffuse scattering. Thermal vibrations (phonons) are always present in a solid and lead to thermal diffuse scattering, an inelastic scattering contribution at all scattering vectors, but particularly pronounced near reciprocal lattice points. The diffuse scattering due to correlations in the local atomic arrangement is called short-range order scattering; the diffuse scattering due to static displacements is called displacement scattering. Small-angle scattering corresponds to the diffuse scattering near the origin of reciprocal space and provides information about long-range concentration fluctuations (while displacement scattering vanishes with $Q \rightarrow 0$).

Throughout this section, scattering intensities are expressed in terms of scattering cross-sections (differential cross-sections without energy analysis, double-differential cross-sections for scattering experiments with energy analysis). To introduce the diffuse scattering including thermal diffuse scattering, the coherent double-differential scattering cross-section is written within the kinematic scattering theory (see e.g. [Squi96])

$$\begin{aligned}
\left(\frac{\mathrm{d}^2\sigma}{\mathrm{d}\Omega \mathrm{d}E} \right)^{\mathrm{coh}} &= \frac{k_{\mathrm{f}}}{k_{\mathrm{i}}} \frac{1}{2\pi\hbar} \sum_{mn} \int_{-\infty}^{\infty} b_m b_n \exp(\mathrm{i}\underline{Q} \cdot [\underline{r}_m - \underline{r}_n]) \\
&\quad \times \langle \exp(\mathrm{i}\underline{Q} \cdot [\underline{u}_m(0) - \underline{u}_n(t)]) \rangle \\
&\quad \times \exp(-\mathrm{i}\frac{E}{\hbar}t)\mathrm{d}t
\end{aligned} \qquad (15)$$

where $\underline{Q} = \underline{k}_f - \underline{k}_i$ is the "momentum transfer" (referred to as scattering vector; $\underline{k}_f$ and $\underline{k}_i$ are the wave vectors of the scattered and incident neutrons) and $E = E_f - E_i$ the energy transfer experienced by the scattered neutron, b_m the coherent scattering length of the atom m, $\underline{r}_m$ the actual (static) position of the atom m given in eq. (7), $\underline{u}_m(t)$ the dynamic displacement of the atom m owing to thermal vibrations and $\langle ... \rangle$ the average with respect to the thermal vibrations.

The thermal average in eq. (15) is given by

$$
\begin{aligned}
\langle \exp(i\underline{Q} \cdot [\underline{u}_m(0) - \underline{u}_n(t)]) \rangle &= \exp(-M_m)\exp(-M_n) \\
&\times \exp\langle [\underline{Q} \cdot \underline{u}_m(0)][\underline{Q} \cdot \underline{u}_n(t)] \rangle
\end{aligned}
\tag{16}
$$

with the species-dependent Debye-Waller factors $\exp(-M_m) = \exp(-Q^2\langle u_m^2(t)\rangle/2)$. In the following, an average Debye-Waller factor $\exp(-M_{\mathrm{dyn}})$ is introduced, identical for all atoms. The expansion of the second term in eq. (16)

$$
\exp\langle [\underline{Q} \cdot \underline{u}_m(0)][\underline{Q} \cdot \underline{u}_n(t)] \rangle = 1 + \langle [\underline{Q} \cdot \underline{u}_m(0)][\underline{Q} \cdot \underline{u}_n(t)] \rangle + \frac{1}{2} \cdots
\tag{17}
$$

used in eq. (15) results in the elastic coherent scattering, the one-phonon scattering and the multiphonon scattering. The Bragg scattering, the short-range order scattering, the displacements scattering and the small-angle scattering are introduced on the basis of the elastic scattering contribution, while the one-phonon scattering is used to approximate thermal diffuse neutron scattering.

2.2.1   Elastic diffuse neutron scattering

Within the static approximation, the elastic scattering is

$$
\left(\frac{\mathrm{d}^2\sigma}{\mathrm{d}\Omega \mathrm{d}E} \right)^{\mathrm{coh}} = \left(\frac{\mathrm{d}\sigma}{\mathrm{d}\Omega} \right)^{\mathrm{coh}} \delta(E)
\tag{18}
$$

with

$$
\left(\frac{\mathrm{d}\sigma}{\mathrm{d}\Omega} \right)^{\mathrm{coh}} = e^{-2M_{\mathrm{dyn}}} \sum_{mn} b_m b_n e^{i\underline{Q}\cdot(\underline{r}_m - \underline{r}_n)}.
\tag{19}
$$

For binary alloys the coherent scattering length b_m of the atom m is expressed in terms of occupation numbers $p_{\underline{r}_m}^\mu$ given in eq. (1).

Bragg and short-range order scattering. Since the positions $\underline{r}_m$ do not depend on time and the static atomic displacements $\underline{\delta}_m$ are assumed to be zero

(average lattice), $\underline{r}_m$ is equal to $\underline{R}_m$ and the elastic coherent differential scattering cross-section per atom is

$$\left(\frac{d\sigma}{d\Omega}\right)^{\text{coh}} = \frac{1}{N}e^{-2M_{\text{dyn}}}\sum_{mn}b_m b_n e^{i\underline{Q}\cdot(\underline{R}_m - \underline{R}_n)}. \tag{20}$$

It is useful to write the positions of the atoms $\underline{R}_m$ in terms of the real-space lattice vectors $\underline{a}_i$, $i = 1, 2, 3$, the scattering vector $\underline{Q}$ in terms of the reciprocal lattice vectors $\underline{a}_i^*$ and the scattering vector $\underline{h} = (h_1, h_2, h_3)$ in reciprocal lattice units (r.l.u.)

$$\underline{R}_m = l\underline{a}_1 + m\underline{a}_2 + n\underline{a}_3 \tag{21}$$

$$\underline{Q} = 2\pi(h_1\underline{a}_1^* + h_2\underline{a}_2^* + h_3\underline{a}_3^*). \tag{22}$$

The Bragg scattering represents one term of this differential scattering cross-section

$$I_{\text{Bragg}}(\underline{h}) = \frac{(2\pi)^3}{v_0}(c_A b_A^2 + c_B b_B^2)e^{-2M_{\text{dyn}}}\sum_{\underline{G}}\delta(\underline{h} - \underline{G}) \tag{23}$$

where v_0 is the volume of the unit cell and $\underline{G}$ a reciprocal lattice vector. Thus, Bragg scattering only occurs when $\underline{h} = \underline{G}$.

In addition, short-order scattering is present for all $\underline{Q}$. The imaginary part of the exponential factor in eq. (20) vanishes because of the symmetry of the average lattice (e.g. $lmn = \bar{l}\overline{mn}$ for cubic structures) and

$$I_{\text{SRO}}(\underline{h}) = c_A c_B|b_A - b_B|^2 e^{-2M_{\text{dyn}}}\sum_{lmn}\alpha_{lmn}\cos(\pi h_1 l)\cos(\pi h_2 m)\cos(\pi h_3 n).(24)$$

For a statistically uncorrelated atomic arrangement, the short-range order scattering devided by $e^{-2M_{\text{dyn}}}$ is constant and is called monotonic Laue scattering (or one Laue unit, L.u.)

$$I_{\text{Laue}}(\underline{h}) = c_A c_B|b_A - b_B|^2. \tag{25}$$

Displacement scattering. Considering the static atomic displacements $\underline{\delta}_m$ from the average lattice sites $\underline{R}_m$ (the actual (static) position being $\underline{r}_m = \underline{R}_m + \underline{\delta}_m$), the differential cross-section (for all $\underline{Q}$) in eq. (19) is given by

$$\left(\frac{d\sigma}{d\Omega}(\underline{Q})\right)^{\text{coh}} = \frac{1}{N}e^{-2M_{\text{dyn}}}\sum_m\sum_n b_m b_{m+n}e^{i\underline{Q}\cdot(\underline{R}_m - \underline{R}_n)}e^{i\underline{Q}\cdot(\underline{\delta}_m - \underline{\delta}_{m+n})}. \tag{26}$$

The displacement scattering can not be represented in a closed form. Often a series expansion of the second term in eq. (26) is used (e.g. Borie and Sparks [Spar66] and

Schwartz and Cohen [Schw87]). To introduce species-dependent static Debye-Waller factors, a cumulant expansion has to be applied (e.g. Dietrich and Fenzl [Diet89]). The exponent of the Debye-Waller factor is then written as $M = M_{\text{dyn}} + M_{\text{sta}}$, where M_{sta} represents an average value as M_{dyn}. To describe the weighting factors due to the coherent scattering lengths b_A and b_B of the displacement scattering contributions, the following parameters are introduced (written to include the case of X-rays where the atomic scattering factors are complex)

$$\eta = \text{Re}\left(\frac{b_A}{b_A - b_B}\right) \tag{27}$$

$$\xi = \text{Re}\left(\frac{b_B}{b_A - b_B}\right) \tag{28}$$

$$\tilde{\eta}^2 = \frac{|b_A|^2}{|b_A - b_B|^2} \tag{29}$$

$$\tilde{\xi}^2 = \frac{|b_B|^2}{|b_A - b_B|^2} \tag{30}$$

$$\tilde{\eta}\tilde{\xi} = \text{Re}\left(\frac{b_A b_B^*}{|b_A - b_B|^2}\right). \tag{31}$$

The elastic diffuse scattering (in Laue units) is the sum of short-range order scattering, linear displacement scattering and quadratic displacement scattering,

$$
\begin{aligned}
\frac{I_{\text{dif}}(\underline{h})}{c_A c_B |b_A - b_B|^2 e^{-2M}} &= I_{\text{SRO}}(\underline{h}) \\
&+ \sum_i h_i [\,\eta Q_i^{\text{AA}}(\underline{h}) + \xi Q_i^{\text{BB}}(\underline{h})] \\
&+ \sum_i h_i^2 [\tilde{\eta}^2 R_i^{\text{AA}}(\underline{h}) + 2\tilde{\eta}\tilde{\xi} R_i^{\text{AB}}(\underline{h}) + \tilde{\xi}^2 R_i^{\text{BB}}(\underline{h})] \\
&+ \sum_{i>j}\sum_j h_i h_j [\tilde{\eta}^2 S_{ij}^{\text{AA}}(\underline{h}) + 2\tilde{\eta}\tilde{\xi} S_{ij}^{\text{AB}}(\underline{h}) + \tilde{\xi}^2 S_{ij}^{\text{BB}}(\underline{h})].
\end{aligned} \tag{32}
$$

The linear displacement Fourier series $Q_i^{\text{AA}}(\underline{h})$ and $Q_i^{\text{BB}}(\underline{h})$ are

$$Q_x^{\text{AA}}(\underline{h}) = -2\pi \sum_{lmn}\left(\frac{c_A}{c_B} + \alpha_{lmn}\right)\langle x_{lmn}^{\text{AA}}\rangle \sin(\pi h_1 l)\cos(\pi h_2 m)\cos(\pi h_3 n) \tag{33}$$

$$Q_x^{\text{BB}}(\underline{h}) = +2\pi \sum_{lmn}\left(\frac{c_B}{c_A} + \alpha_{lmn}\right)\langle x_{lmn}^{\text{BB}}\rangle \sin(\pi h_1 l)\cos(\pi h_2 m)\cos(\pi h_3 n), \tag{34}$$

and the quadratic displacement scattering Fourier series for, e.g., the AA and AB

pairs are

$$R_x^{AA}(\underline{h}) = -2\pi^2 \sum_{lmn} (\frac{c_A}{c_B} + \alpha_{lmn}) \langle x_{000}^A x_{lmn}^A \rangle \cos(\pi h_1 l) \cos(\pi h_2 m) \cos(\pi h_3 n) \quad (35)$$

$$R_x^{AB}(\underline{h}) = -2\pi^2 \sum_{lmn} (1 - \alpha_{lmn}) \langle x_{000}^A x_{lmn}^B \rangle \cos(\pi h_1 l) \cos(\pi h_2 m) \cos(\pi h_3 n) \quad (36)$$

$$S_{xy}^{AA}(\underline{h}) = +4\pi^2 \sum_{lmn} (\frac{c_A}{c_B} + \alpha_{lmn}) \langle x_{000}^A y_{lmn}^A \rangle \sin(\pi h_1 l) \sin(\pi h_2 m) \cos(\pi h_3 n) \quad (37)$$

$$S_{xy}^{AB}(\underline{h}) = +4\pi^2 \sum_{lmn} (1 - \alpha_{lmn}) \langle x_{000}^A y_{lmn}^B \rangle \sin(\pi h_1 l) \sin(\pi h_2 m) \cos(\pi h_3 n). \quad (38)$$

Evaluation procedure. A central task in diffuse scattering investigations is the separation of the various scattering contributions. Diffuse X-ray scattering data were approximated using short-range order parameters α_{lmn} and the fitting parameters for the displacement scattering of, e.g., pairs of type AA and AB

$$\gamma_{lmn,x}^{AA} = -2\pi\eta(\frac{c_A}{c_B} + \alpha_{lmn}) \langle x_{lmn}^A - x_{000}^A \rangle \tag{39}$$

$$\delta_{lmn,x}^{AA} = -2\pi^2\tilde{\eta}^2(\frac{c_A}{c_B} + \alpha_{lmn}) \langle x_{000}^A x_{lmn}^A \rangle \tag{40}$$

$$\delta_{lmn,x}^{AB} = -2\pi^2\tilde{\eta}\tilde{\xi}(1 - \alpha_{lmn}) \langle x_{000}^A x_{lmn}^B \rangle \tag{41}$$

$$\epsilon_{lmn,xy}^{AA} = +2\pi^2\tilde{\eta}^2(\frac{c_A}{c_B} + \alpha_{lmn}) \langle x_{000}^A y_{lmn}^A \rangle \tag{42}$$

$$\epsilon_{lmn,xy}^{AB} = +4\pi^2\tilde{\eta}\tilde{\xi}(1 - \alpha_{lmn}) \langle x_{000}^A y_{lmn}^B \rangle. \tag{43}$$

Measuring scattering intensities at more than 25 symmetry-equivalent positions within a three-dimensional minimal volume of reciprocal space, allows the species-dependent static atomic displacements $\langle x_{lmn}^\mu - x_{000}^\mu \rangle$ and the species-dependent correlations $\langle x_{000}^\mu y_{lmn}^\nu \rangle$ to be determined. This separation procedure exploits the $|\underline{h}|$-dependence of the atomic scattering factors for X-ray scattering.

Three evaluation procedures may be distinguished; (*i*) separate the various terms in eq. (32) before determining the Fourier coefficients for each term (e.g. Georgopoulos-Cohen method [Geor77]); (*ii*) fit directly the leading Fourier coefficients (first implemented by Williams [Will72] and summarized in appendix E); (*iii*) separate the quadratic displacement scattering on the basis of additional experimental information before determining the Fourier coefficients for the short-range order and linear displacement scattering (3λ-method referred to in [Jian96]).

The separation of scattering contributions contained in the elastic diffuse neutron scattering is restricted to 10 terms, as the scattering lengths b_m do not depend

markedly on the scattering vector $\underline{h}$. The Fourier series accessible are

$$Q_i(\underline{h}) = \eta Q_i^{\mathrm{AA}}(\underline{h}) + \xi Q_i^{\mathrm{BB}}(\underline{h}) \tag{44}$$

$$R_i(\underline{h}) = \tilde{\eta}^2 R_i^{\mathrm{AA}}(\underline{h}) + 2\tilde{\eta}\tilde{\xi} R_i^{\mathrm{AB}}(\underline{h}) + \tilde{\xi}^2 R_i^{\mathrm{BB}}(\underline{h}) \tag{45}$$

$$S_{ij}(\underline{h}) = \tilde{\eta}^2 S_{ij}^{\mathrm{AA}}(\underline{h}) + 2\tilde{\eta}\tilde{\xi} S_{ij}^{\mathrm{AB}}(\underline{h}) + \tilde{\xi}^2 S_{ij}^{\mathrm{BB}}(\underline{h}). \tag{46}$$

The species-averaged fitting parameters are then given by

$$\gamma_{lmn}^x = \gamma_{lmn,x}^{\mathrm{AA}} - \gamma_{lmn,x}^{\mathrm{BB}} \tag{47}$$

$$\delta_{lmn}^x = \delta_{lmn,x}^{\mathrm{AA}} + \delta_{lmn,x}^{\mathrm{BB}} + \delta_{lmn,x}^{\mathrm{AB}} + \delta_{lmn,x}^{\mathrm{BA}} \tag{48}$$

$$\epsilon_{lmn}^{xy} = \epsilon_{lmn,xy}^{\mathrm{AA}} + \epsilon_{lmn,xy}^{\mathrm{BB}} + \epsilon_{lmn,xy}^{\mathrm{AB}} + \epsilon_{lmn,xy}^{\mathrm{BA}} \tag{49}$$

Adequate evaluation procedures are the separation method of Borie and Sparks [Spar66] and the least-squares fitting implemented by Williams [Will72]. To determine species-dependent static atomic displacements in a neutron scattering experiment, measurements of the elastic diffuse neutron scattering of two single crystals with different isotopic content, but identical microstructure would be required.

2.2.2 Small-angle neutron scattering

Small-angle scattering (in the region close to the origin of reciprocal space) is caused by the variation of the scattering length density over distances exceeding the interatomic distances in crystalline solids. Details on a scale smaller than the size of the unit cell will not be resolved and the discrete arrangement of scatterers in eq. (20) may be replaced by a continuous distribution $\rho(\mathbf{r})$ of scattering lengths, called scattering length density. The small-angle scattering cross-section per atom is given by

$$\left(\frac{\mathrm{d}\sigma}{\mathrm{d}\Omega}\right)^{\mathrm{SAS}} = \frac{1}{N}\left|\int_{V_{\mathrm{s}}} \rho(\underline{r}) \exp(i\underline{Q} \cdot \underline{r})\mathrm{d}^3\underline{r}\right|^2, \tag{50}$$

where N is the number of scattering centers in the sample volume V_{s}. The fluctuation in the scattering length density is

$$\Delta\rho(\underline{r}) = \rho(\underline{r}) - \overline{\rho(\underline{r})} \tag{51}$$

taking the scattering length density $\overline{\rho(\underline{r})}$ as reference, averaged over distances larger than $1/Q_{\min}$ ($Q_{\min}$ being the minimal scattering vector where small-angle scattering intensities were registered in the experiment). Then, the small-angle scattering cross-section is

$$\left(\frac{\mathrm{d}\sigma}{\mathrm{d}\Omega}\right)^{\mathrm{SAS}} = \frac{1}{N}\left|\int_{V_{\mathrm{s}}} \Delta\rho(\underline{r}) \exp(i\underline{Q} \cdot \underline{r})\mathrm{d}^3\underline{r}\right|^2. \tag{52}$$

Further details may be found, e.g. in [Kost96].

2.2.3   Thermal diffuse neutron scattering

Kothari and Singwi [Koth59] calculated the total thermal diffuse scattering cross-section σ_{TDS} and

$$\left(\frac{\mathrm{d}\sigma}{\mathrm{d}\Omega}\right)^{\mathrm{TDS}} = \frac{\sigma_{\mathrm{TDS}}}{4\pi}\exp(-2M), \tag{53}$$

using the following assumptions:

(*i*) The thermal diffuse scattering is basically one-phonon scattering.

(*ii*) The coherent and incoherent one-phonon scattering cross-sections are written as

$$\left(\frac{\mathrm{d}^2\sigma}{\mathrm{d}\Omega\mathrm{d}E}\right)^{\mathrm{coh}} = \sigma_{\mathrm{coh}}\exp(-2M)F_{\mathrm{coh}}(\underline{Q},\omega) \tag{54}$$

$$\left(\frac{\mathrm{d}^2\sigma}{\mathrm{d}\Omega\mathrm{d}E}\right)^{\mathrm{inc}} = \sigma_{\mathrm{inc}}\exp(-2M)F_{\mathrm{inc}}(\underline{Q},\omega), \tag{55}$$

where $F_{\mathrm{coh}}(\underline{Q},\omega)$ and $F_{\mathrm{inc}}(\underline{Q},\omega)$ are scattering functions that do not describe the interaction of the neutron with the atoms, but the relative positions of the atoms in the scattering system and their motion. Integrated over the solid angle $\mathrm{d}\Omega$, $F_{\mathrm{coh}}(\underline{Q},\omega)$ is assumed to be equal to $F_{\mathrm{inc}}(\underline{Q},\omega)$, a procedure that is referred to as incoherent approximation. Then, the total thermal diffuse scattering cross-section is

$$\sigma_{\mathrm{TDS}} = (\sigma_{\mathrm{coh}} + \sigma_{\mathrm{inc}})\int F_{\mathrm{inc}}(\underline{Q},\omega)\mathrm{d}\omega. \tag{56}$$

(*iii*) The coherent and incoherent one-phonon scattering is proportional to the squared scalar product of the scattering vector $\underline{Q}$ and the polarisation $\underline{e}_s$ of a particular vibration mode s. The sum over all lattice modes s is expressed within the Debye approximation by the density of states $Z(\omega) = 3\hbar^2\omega^2/(k_{\mathrm{B}}\theta_{\mathrm{D}})^3$ and the Debye temperature θ_{D}

$$\sum_s \frac{|(\underline{k}_{\mathrm{i}} - \underline{k}_{\mathrm{f}})\cdot\underline{e}_s|^2}{\omega_s} = (\underline{k}_{\mathrm{i}} - \underline{k}_{\mathrm{f}})^2 N\frac{3\hbar^2\omega}{(k_{\mathrm{B}}\theta_{\mathrm{D}})^3} \tag{57}$$

for phonon emission and phonon absorption.
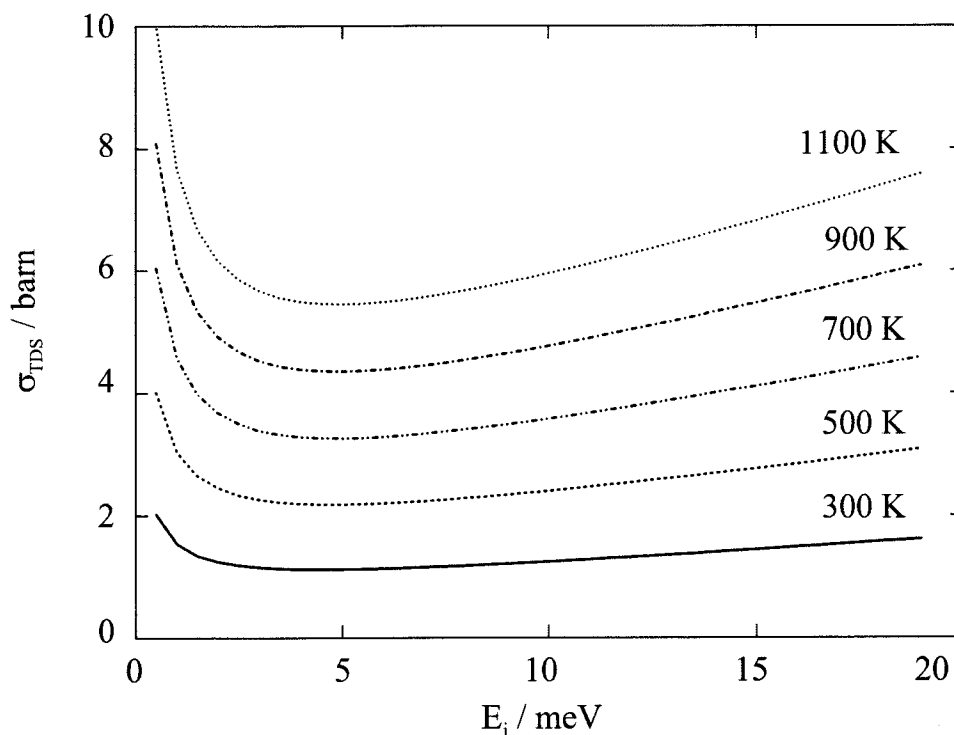
Fig. 3: Thermal diffuse scattering cross-section σ_{TDS} calculated for ^{58}Ni-8.4 at.% Au using eq. (58) [Koth59].

The integration with respect to the energy transfer $\hbar\omega$ is converted into an integration over E_{f} and the total thermal diffuse scattering is

$$
\begin{aligned}
\sigma_{\mathrm{TDS}} \;=\;& \frac{3(\sigma_{\mathrm{coh}} + \sigma_{\mathrm{inc}})m}{M}\left(\frac{T}{\theta_{\mathrm{D}}}\right)^2 \frac{E_{\mathrm{i}}}{k_{\mathrm{B}}\theta_{\mathrm{D}}} \\
&\times \int_0^{\theta_{\mathrm{D}}/T}\left(1 + z\frac{k_{\mathrm{B}}T}{E_{\mathrm{i}}}\right)^{\frac{1}{2}}\left(2 + z\frac{k_{\mathrm{B}}T}{E_{\mathrm{i}}}\right)\frac{z}{e^z - 1}\mathrm{d}z,
\end{aligned}
\qquad (58)
$$

where m is the mass of the neutron and M the averaged mass of the atoms.

For all temperatures, the thermal diffuse scattering cross-section of ^{58}Ni-8.4 at.% Au (see Fig. 3) has a minimal value at about 5 meV for the energy of the incident neutrons. For thermal neutron energies E_{i}, the value of σ_{TDS} varies approximately linearly with the sample temperature.

2.3   Modeling and ordering energies

In order to investigate the physical properties of a local atomic arrangement, crystals of typically $32 \times 32 \times 32$ fcc (or bcc) unit cells were modeled based on a set of short-range order parameters. Typical elements of ordered structures are determined by configurational analysis of model crystals. Such model crystals are also the basis for the determination of effective pair interaction parameters using the inverse Monte Carlo method. From these effective pair interaction parameters, ordering energies are determined and possible ground state structures can be assessed.

Model crystals. Gehlen and Cohen [Gehl65] introduced a procedure for modeling crystals from a set of short-range order parameters. Starting from a crystal representing a statistically uncorrelated local atomic arrangement, a minority and a majority atom are exchanged, and short-range order parameters are calculated until the short-range order parameters of the finally modeled crystal lie within the statistical errors of the experimental data. As an example, Fig. 4 shows the local atomic arrangement on $\{111\}$ planes of Ni-rich Ni-Au for a statistically uncorrelated and a short-range decomposed model crystal. While in the short-range decomposed state small groups of minority atoms (Au) are characteristic, in the statistically uncorrelated arrangement, the minority atoms are less frequently surrounded by other minority atoms.

(a)   (b)
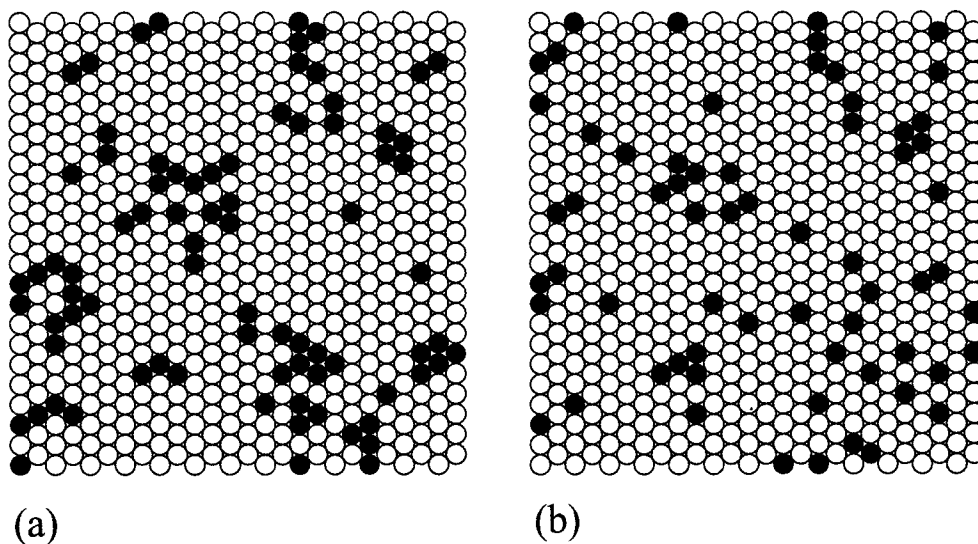
Fig. 4: A $\{111\}$ plane of ^{58}Ni-8.4 at.% Au. (a) Equilibrium state at 1083 K, (b) statistically uncorrelated arrangement (open circles: Ni atoms; filled circles: Au atoms).

Configurational analysis. As in solid solutions local configurations for precipitates or ordered structures are expected, the model crystals were searched for characteristic configurations. Clapp [Clap71] introduced a nomenclature that describes all possible nearest-neighbor configurations (Clapp configurations) for bcc or fcc structures of a binary alloy. Two quantities are attributed to each Clapp configuration: (i) its abundance with respect to the total number of configurations and (ii) the enhancement factor defined as the ratio of the abundances between the actual atomic arrangement and a statistically uncorrelated one. Model crystals may be searched for possible (i) superstructures or (ii) agglomerates of minority atoms.

Superstructures. Long-range ordered, stoichiometric structures are characterized by a few typical nearest-neighbor configurations. The $L1_2$ superstructure, for example, is characterized by the Clapp configuration C16 (see Fig. 5). In substoichiometric, but still ordered configurations, minority atoms are replaced by majority atoms. Therefore, typical sequences can be found, classifying these configurations using the number of replaced minority atoms as a criterion. For substoichiometric $L1_2$ superstructures the sequence C16 $\rightarrow$ C7 $\rightarrow$ C3, C4 is characteristic (see Fig. 5). If configurations of such sequences have large enhancement factors and large abundances, the corresponding superstructure is expected to describe the stable low-temperature state.
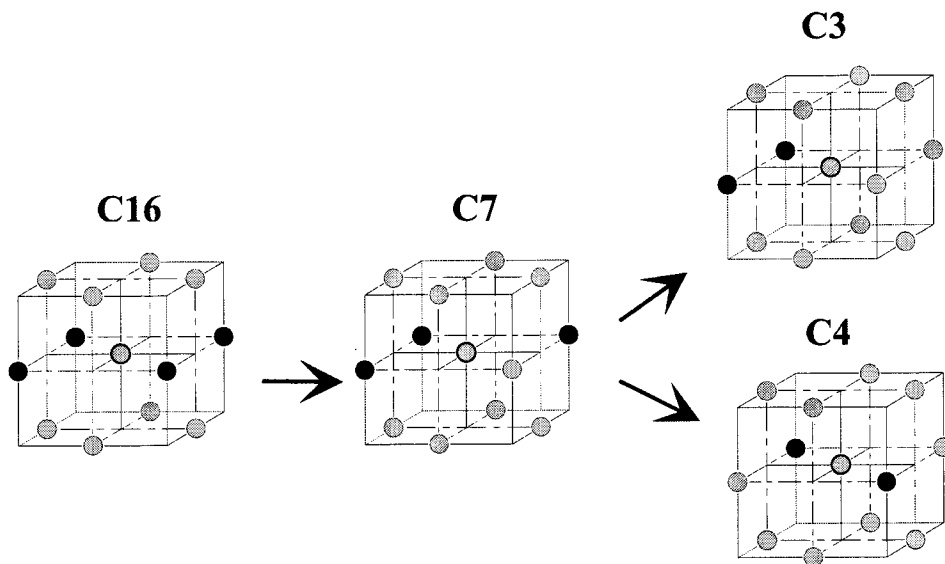

Fig. 5: Clapp configuration C16, describing the perfectly ordered, stoichiometric $L1_2$ structure. For sub-stoichiometric $L1_2$, the sequence C16 $\rightarrow$ C7 $\rightarrow$ C3, C4 is characteristic.

Agglomerates of minority atoms. In order to get the shape of the agglomerates, the case of minority atoms around minority atoms is investigated. Configurations such as platelets, rods or tetrahedrons can be distinguished. The arrangement of these configurations (e.g. platelets on $\{100\}$ planes) is irregular and does not correspond to the periodic sequence of platelets on (100) planes as observed for example, for the long-range ordered $L1_0$ structure.

Ordering energy. The local atomic arrangement of states in thermal equilibrium (represented by model crystals) can be parameterized by a generalized Ising Hamiltonian H. The input parameters for the Monte Carlo simulation (see appendix B) are the effective pair interaction parameters calculated from model crystals using the inverse Monte Carlo method (see appendix C). In the following, first a Hamiltonian for local atomic arrangements is presented, then a Hamiltonian taking the static atomic displacements explicitly into account.

Let the energy of formation H of any atomic arrangement be represented by a series expansion up to second order in the site occupation numbers $p_{\underline{r}}^\mu$,

$$H \;=\; H_0 + \sum_{\underline{r}} \sum_{\nu} V_{\underline{r}}^{\nu} p_{\underline{r}}^{\nu} + \frac{1}{2} \sum_{\mu\nu} \sum_{\underline{r}\,\underline{r}+d\underline{r}} V_{d\underline{r}}^{\mu\nu} p_{\underline{r}}^{\nu} p_{\underline{r}+d\underline{r}}^{\mu}, \tag{59}$$

where $V_{\underline{r}}^{\nu}$ are the chemical potentials of the component ν and $V_{d\underline{r}}^{\mu\nu}$ are the species-dependent pair interaction parameters for the atoms μ and ν at the lattice sites $\underline{r}$ and $\underline{r} + d\underline{r}$.

The first two terms in eq. (59) represent the energy of a statistically uncorrelated atomic arrangement,

$$H_0 + \sum_{\underline{r}} \sum_{\nu} V_{\underline{r}}^{\nu} p_{\underline{r}}^{\nu} \;=\; H_0 + NV^{\mathrm{A}}(1 - c_{\mathrm{B}}) + NV^{\mathrm{B}} c_{\mathrm{B}} \tag{60}$$

where N is the number of atoms. The third term is given by

$$\frac{1}{2} \sum_{\mu\nu} \sum_{\underline{r}\,\underline{r}+d\underline{r}} V_{d\underline{r}}^{\mu\nu} p_{\underline{r}}^{\nu} p_{\underline{r}+d\underline{r}}^{\mu} \;=\; \frac{N}{2} \sum_{d\underline{r}} \left[(1 - c_{\mathrm{B}})^2 V_{d\underline{r}}^{\mathrm{AA}} + c_{\mathrm{B}}^2 V_{d\underline{r}}^{\mathrm{BB}} + 2 c_{\mathrm{B}}(1 - c_{\mathrm{B}}) V_{d\underline{r}}^{\mathrm{AB}} \right]$$

$$+ \; \frac{N}{2} c_{\mathrm{B}}(1 - c_{\mathrm{B}}) \sum_{d\underline{r}} \left[V_{d\underline{r}}^{\mathrm{AA}} + V_{d\underline{r}}^{\mathrm{BB}} - 2 V_{d\underline{r}}^{\mathrm{AB}} \right] \alpha_{d\underline{r}}. \tag{61}$$

Thus, the energy of formation H is given by two contributions; the first only depends on the overall composition and only the second on the local atomic arrangement. The latter term is referred to as the ordering energy

$$\Delta H_{\mathrm{ord}}/N = c_{\mathrm{A}} c_{\mathrm{B}} \sum_{d\underline{r}} \alpha_{d\underline{r}} V_{d\underline{r}} \tag{62}$$

with the effective pair interaction parameters

$$V_{d\underline{r}} = \frac{1}{2}\left(V_{d\underline{r}}^{AA} + V_{d\underline{r}}^{BB} - 2V_{d\underline{r}}^{AB}\right).$$ (63)

Cook and de Fontaine [Cook69] introduced a series expansion up to second order in the site occupation numbers $p_{\underline{r}}^{\nu}$ and the components of the species-dependent static atomic displacements $\delta_{\underline{r}}^{\alpha}$

$$
\begin{aligned}
H &= H_0 + \sum_{\underline{r}}\sum_{\nu} V_{\underline{r}}^{\nu} p_{\underline{r}}^{\nu} + \frac{1}{2}\sum_{\mu\nu}\sum_{\underline{r}\,\underline{r}+d\underline{r}} V_{d\underline{r}}^{\mu\nu} p_{\underline{r}}^{\nu} p_{\underline{r}+d\underline{r}}^{\mu} \\
&+ \sum_{\alpha}\sum_{\mu\nu}\sum_{\underline{r}\,\underline{r}+d\underline{r}} \Phi_{d\underline{r}}^{\alpha}(\delta_{\underline{r}}^{\alpha} p_{\underline{r}}^{\mu} p_{\underline{r}+d\underline{r}}^{\nu} - p_{\underline{r}}^{\mu}\delta_{\underline{r}+d\underline{r}}^{\alpha} p_{\underline{r}+d\underline{r}}^{\nu}) \\
&+ \frac{1}{2}\sum_{\alpha\beta}\sum_{\mu\nu}\sum_{\underline{r}\,\underline{r}+d\underline{r}} \Phi_{d\underline{r}}^{\alpha\beta} p_{\underline{r}}^{\mu} p_{\underline{r}+d\underline{r}}^{\nu}\delta_{\underline{r}}^{\alpha}\delta_{\underline{r}+d\underline{r}}^{\beta},
\end{aligned}
$$ (64)

where $\Phi_{d\underline{r}}^{\alpha}$ are the solute-lattice coupling parameters and $\Phi_{d\underline{r}}^{\alpha\beta}$ the lattice coupling parameters. Assuming thermal equilibrium on a completely relaxed lattice, the sum of all forces on the atoms is zero and the three terms in $p_{\underline{r}}^{\mu} p_{\underline{r}+d\underline{r}}^{\nu}$ can be rewritten in one term. The Hamiltonian H then has a form similar to eq. (59), and the effective pair interaction parameters are interpreted as

$$V_{d\underline{r}} = V_{d\underline{r}}^{ideal} + V_{d\underline{r}}^{rel}$$ (65)

where $V_{d\underline{r}}^{ideal}$ are the effective pair interaction parameters describing the average lattice and $V_{d\underline{r}}^{rel}$ those describing the static displacements due to different atomic sizes of the constituents. Thus, experimentally determined coupling parameters $\Phi_{d\underline{r}}^{\alpha}$ and $\Phi_{d\underline{r}}^{\alpha\beta}$ provide direct access to the quantity $V_{d\underline{r}}^{rel}$.

Effective pair interaction parameters. If the local atomic arrangement in thermal equilibrium is characterized by a representative set of short-range order parameters α_{lmn}, the effective pair interaction parameters can be calculated from model crystals using either mean-field statistical mechanics or the inverse Monte Carlo method (see appendix C). Mean-field statistical mechanics gives an expression (referred to as Krivoglaz-Clapp-Moss approximation [Clap66, Kriv69a]) relating the Fourier transform $I_{SRO}(\underline{h})$ of the short-range order parameters to the Fourier transform $\tilde{V}(\underline{h})$ of the effective pair interaction parameters

$$I_{SRO}(\underline{h}) = \frac{1}{1 + 2c_A c_B \tilde{V}(\underline{h})/k_B T}.$$ (66)

Depending on the effective pair interaction parameters, the local atomic arrangement of solid solutions can be classified into short-range ordered, short-range decomposed

and statistically uncorrelated arrangements. Maxima in $I_{\text{SRO}}(\underline{h})$, for example, correspond to minima in $\tilde{V}(\underline{h})$, and a short-range ordered atomic arrangement.

3 Experimental

3.1 Sample preparation

Starting material for the sample preparation was 5N+ gold (Métaux Précieux SA METALOR, Neuchâtel, Switzerland) and isotopically pure (99.86 at.%) ^{58}Ni (State Scientific Center, Moscow, Russia). The isotopic content and the content of other elements as certified by the company are given in Table 1. The purity of the Ni-58 isotope, being crucial in the neutron scattering experiments, was verified using mass spectroscopy (Dr. M. Döbeli, ETH Zürich). The isotope, delivered as a powder, was first arc-melted and solidified as small spheres. The alloying with gold was performed in an induction melting furnace in order to get a homogeneous starting material for the subsequent crystal growth using the Bridgman technique.

Gold has a large absorption cross-section for thermal neutrons (see Table 11 in appendix D) and X-rays. Only for ^{58}Ni-rich ^{58}Ni-Au alloys ($c_{Au} \leq 20$ at.% Au), the ideal thickness d of a sample (at $E_i = 14.68$ meV) is larger than 2 mm. A diameter of 8 mm (cylindrically shaped sample) is suited to investigate the diffuse neutron scattering of ^{58}Ni-10 at.% Au; for ^{58}Ni-60 at.% Au, a diameter of 2 mm was chosen.

The experimental parameters for crystal growth were determined using binary alloys of ^{nat}Ni-10 at.% Au, and a standard procedure was developed. A ^{58}Ni-10 at.% Au single crystal was grown by the Bridgman technique (velocity of growth of 0.7 mm/h). Any further speed led to the appearance of dendrites. As in any

Table 1: Abundance of the isotopes and content of other elements certified for the ^{58}Ni powder used in the sample preparation.

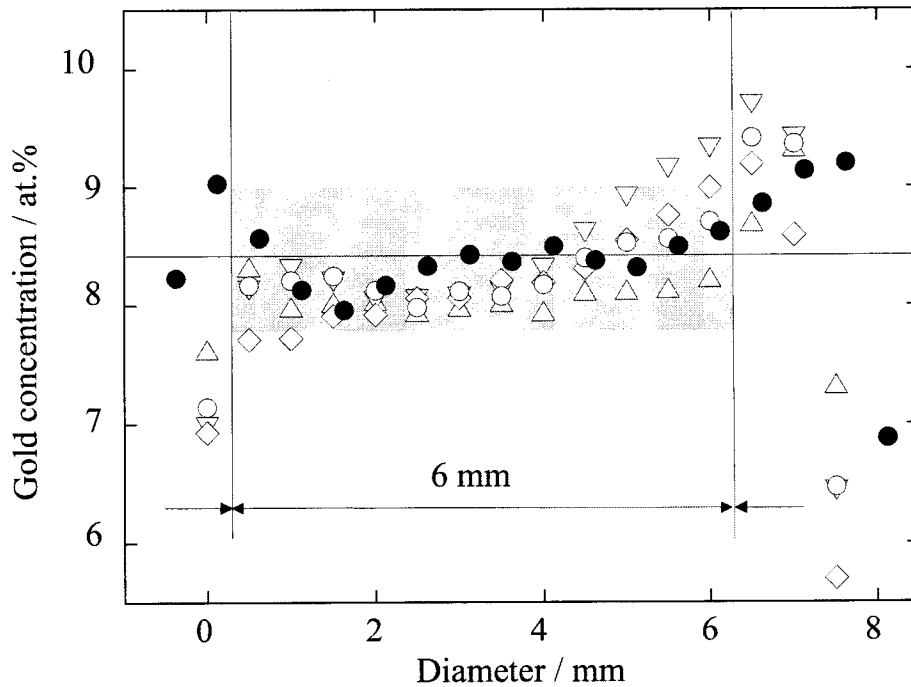| isotope	abundance [at.%]	element	content [wt.%]	element	content [wt.%]
58	99.86	Cu	0.01	Pb	0.003
60	0.13	Ca	0.004	Si	0.003
61		Fe	0.003	Al	<0.002
62	0.01	Mg	0.003	Cd	<0.001
64		Na	0.003	K	<0.001

Fig. 6: Gold concentration on the top (open symbols) and the bottom (•) face of the cylindrical ^{58}Ni-8.4 at.% Au sample used for wide-angle neutron scattering. Four scans were measured on the top face rotating the sample by 0° (o), 45° (▽), 90° (△) and 135° (◊). Edge effects due to a beam size of 1 mm^2 restrict the usable range to 6 mm. The grey area stands for the width of the standard deviation over 50 values.

neutron scattering experiment, a small concentration gradient and a high quality of the single crystal are important. In order to check for concentration gradients and to determine the absolute concentration, energy dispersive X-ray fluorescence analysis (TX 5000, Spectrace Instruments, California, USA) was employed. Two polycrystalline standards with nominal compositions of Ni-8 at.% Au and Ni-12 at.% Au were used to determine absolute concentrations by linear interpolation. On the basis of line scans along the growth axis, a cylindrically shaped sample with a diameter and height of 8 mm was selected and cut out of the as-grown single crystalline ingot using spark erosion. Within the resolution of the X-ray fluorescence analysis (∼1 mm in space, ∼0.4 at.% Au in concentration), no concentration gradient along the growth axis was detected. For the area perpendicular to the growth axis, a small concentration gradient is present (see Fig. 6). The values are within the error bar of the absolute concentration of ^{58}Ni-8.4(4) at.% Au, using the standard deviation over 50 individual positions. The cylinder axis of the sample is near ⟨421⟩. This orientation is suited for diffuse scattering experiments, as the main

cubic directions can be reached within about 25° in tilt on an Eulerian cradle.

The adjacent, not completely monocrystalline part was used to prepare a poly-crystalline plate for small-angle neutron scattering. After plastic deformation and recrystallization at 873 K (final average grain size ~50 μm), two disk-shaped samples, 10 mm in diameter and 2.74(2) mm in thickness, were prepared. The absolute concentration was 8.3(4) at.% Au. To compare an as-quenched state with a state in thermal equilibrium at 1173 K, one of the samples was annealed at 1173 K during 5 days and quenched in brine.

The [58]Ni-60 at.% Au single crystal was grown by the Bridgman technique (velocity of growth 0.7 mm/h). The cylindrically shaped sample cut out of the as-grown single crystalline ingot had a diameter of 2 mm and a height of 10 mm. The cylinder axis of the sample was near ⟨421⟩. The fundamental Bragg reflection 200 was reached within 15° in tilt on an Eulerian cradle.

The polycrystalline sample was a plate with a diameter of 10 mm and a thickness of 0.5 mm. It was prepared from the not completely monocrystalline part of [58]Ni-8.4 at.% Au adding gold to reach the final concentration of [58]Ni-60 at.% Au. To compare an as-quenched state with a state in thermal equilibrium at 1173 K, the sample was annealed at 1173 K during 6 days and quenched in brine.

3.2 Small-angle neutron scattering

3.2.1 Set-up at SANS-I

The small-angle scattering of [58]Ni-8.3 at.% Au and [58]Ni-60 at.% Au was measured at various temperatures near and within the miscibility gap using a high-temperature furnace (see Fig. 7). This high-temperature furnace had been successfully used in previous small-angle scattering experiments [Komp01]. Only a summary is given in the following. The furnace is decoupled from the detector and the collimation vessel (two Al windows, 0.3 mm in thickness) to guarantee high-vacuum conditions during the aging processes at elevated temperatures. The beam-defining aperture (6 mm in diameter) incorporated in the furnace, is about 1.5 cm in front of the sample. The sample holder is mounted on a vertical translation table to adjust the sample with respect to the beam-defining aperture. At elevated temperatures, the length of the sample holder significantly increases owing to thermal expansion, and the adjustment of the sample versus the aperture had to be repeated. The temperature is measured near the sample on the sample holder.

The small-angle scattering experiments were performed on the small-angle scattering instrument SANS-I (PSI, Villigen, Switzerland). SANS-I (see Fig. 7) is supplied with neutrons from the spallation source SINQ (PSI, Switzerland). The neutrons are moderated at 25 K by heavy water (resulting in a neutron flux distribution with an average energy of 2.2 meV). These neutrons are guided to the location of the small-angle scattering instrument using neutron guides (50 mm × 50 mm in diameter). A mechanical velocity selector was used providing a wavelength resolution of 10%. Since metastable $L1_0$-ordered precipitates are proposed by Zhao and Notis [Zhao99] for Ni-Au, a wavelength of 8.0(8) Å was chosen to avoid multiple Bragg scattering. The sample-to-detector distance was set to 2 m, corresponding to a scattering vector range of 0.02 to 0.24 Å^{-1}. The collimation length was set to 4.5 m. Scattering intensities were registered by a two-dimensional position-sensitive ^{3}He detector (gas filling: ^{3}He and CF_4 under partial gas pressures of 2.3 and 0.7 bar). The number of the detector elements (7.5 mm × 7.5 mm) is defined by 128 × 128 wires. The direct beam was masked by a beam stop (boron carbide, 85 mm × 85 mm). Data were taken under monitor control.

To convert the small-angle scattering intensities of ^{58}Ni-8.3 at.% Au to absolute scattering cross-sections, the elastic incoherent scattering of a vanadium single crystal (thickness of 2.83 mm) was registered at room temperature. The background was measured without sample (empty configuration) and with a boron nitride sample (thickness of 3.0 mm).
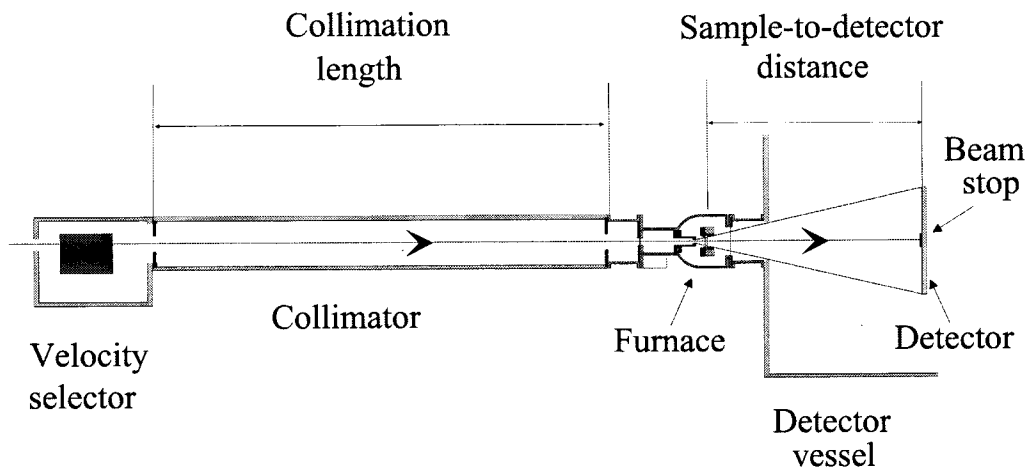

Fig. 7: Small-angle scattering configuration used in the experiment. The distance between velocity selector and collimator is not to scale as the complete collimator device has a total length of 40 m.

3.2.2   Data corrections and calibration

All registered two-dimensional scattering patterns were corrected for background
due to the sample environment and the detector electronics using

$$\frac{I_{\mathrm{S}}^{\mathrm{cor}}(\underline{Q})}{L_{\mathrm{S}}} = \frac{I_{\mathrm{S}}(\underline{Q})}{L_{\mathrm{S}}} - \frac{I_{\mathrm{Abs}}(\underline{Q})}{L_{\mathrm{Abs}}} - A\left[\frac{I_{\mathrm{E}}(\underline{Q})}{L_{\mathrm{E}}} - \frac{I_{\mathrm{Abs}}(\underline{Q})}{L_{\mathrm{Abs}}}\right], \tag{67}$$

where I_i are the as-measured scattering intensities and L_i the monitor counts of
the sample (S), the boron nitride sample (Abs) and the empty configuration (E).
The transmission factor A describes the beam-attenuating processes (coherent and
incoherent scattering as well as true absorption). For a thin slice with a linear
absorption coefficient

$$\mu = \frac{s}{a^3}\left(\sigma_{\mathrm{coh}} + \sigma_{\mathrm{inc}} + \sigma_{\mathrm{abs}}\frac{\lambda}{1.798\mathrm{\AA}} + \sigma_{\mathrm{TDS}}\right) \tag{68}$$

the transmission factor A is given by

$$A = \exp(-\mu d) \tag{69}$$

where s is the number of atoms in the cubic unit cell, a the lattice parameter,
d the sample thickness, σ_{coh} the elastic coherent scattering cross-section, σ_{inc} the
elastic incoherent scattering cross-section, σ_{abs} the absorption cross-section and σ_{TDS}
the scattering cross-section due thermal diffuse scattering. The elastic coherent
scattering cross-section σ_{coh} does not include Bragg scattering, since no fundamental
reflection was excited. For the 110 fundamental reflections of Ni-Au (fcc unit cell),
the Bragg cut-off condition

$$\frac{\lambda}{2a}\sqrt{2} \gg \sin(\theta_{\max}) = 1 \tag{70}$$

is fulfilled if the wavelength λ is larger than 5.1 Å (as in the present experiment
with $\lambda = 8$ Å). The thermal diffuse scattering of ^{58}Ni-8.3 at.% Au has to be taken
into consideration in the linear absorption coefficient and is calculated using eq. (58)
[Koth59]; at elevated temperatures the transmission factor A is significantly reduced
(see section 4.3).

The detector of SANS-I registers inelastically and elastically scattered neutrons
since no energy analysis is performed after the sample. The background-corrected
scattering intensities I_i^{cor}/L_i of the sample (S) and vanadium (V) registered within
a solid angle $\Delta\Omega$ and an energy range ΔE are

$$\frac{I_i^{\mathrm{cor}}/L_i}{\Phi\Delta\Omega\Delta E} = A_i V_i \int_0^\infty f(E_{\mathrm{f}})\frac{\mathrm{d}\Sigma_i^2}{\mathrm{d}\Omega\mathrm{d}E_{\mathrm{f}}}\mathrm{d}E_{\mathrm{f}}, \tag{71}$$

where V_i is the (illuminated) sample volume. The neutron flux Φ is the intensity of the incoming neutron beam per illuminated area on the sample. As the detector efficiency $f(E_f)$ for scattered neutrons with a final energy E_f and the flux Φ can not be determined experimentally with high accuracy, one also measures the incoherent scattering of vanadium. Thus, the macroscopic differential scattering cross-section of the sample is

$$\left(\frac{\mathrm{d}\Sigma}{\mathrm{d}\Omega}\right)_S = \frac{L_V}{L_S}\frac{d_V}{d_S}\frac{A_V}{A_S}\frac{I_S^{\mathrm{cor}}}{I_V^{\mathrm{cor}}}\left(\frac{\mathrm{d}\Sigma}{\mathrm{d}\Omega}\right)_V. \tag{72}$$

In order to compare the wide-angle and the small-angle neutron scattering intensities, the macroscopic scattering cross-section in eq. (72) was converted to the (microscopic) scattering cross-section per atom in the volume a_i^3 of the cubic unit cell using

$$\left(\frac{\mathrm{d}\Sigma_i}{\mathrm{d}\Omega}\right) = \frac{s_i}{a_i^3}\left(\frac{\mathrm{d}\sigma_i}{\mathrm{d}\Omega}\right) \tag{73}$$

and converted to Laue units (L. u.) using the monotonic Laue scattering of a statistically uncorrelated local atomic arrangement (see section 2.2.1). Additionally, the elastic incoherent scattering of the sample was subtracted. Then, the microscopic scattering cross-section for small-angle scattering is

$$\left(\frac{\mathrm{d}\sigma}{\mathrm{d}\Omega}\right)_S^{\mathrm{SANS}} = \frac{1}{c_A c_B |b_A - b_B|^2}\left[\frac{a_S^3}{s_S}\frac{s_V}{a_V^3}\frac{L_V}{L_S}\frac{d_V}{d_S}\frac{A_V}{A_S}\frac{I_S^{\mathrm{cor}}}{I_V^{\mathrm{cor}}}\frac{\sigma_{\mathrm{inc},V}}{4\pi}\right.$$
$$\left. -c_A\sigma_{\mathrm{inc},A} - c_B\sigma_{\mathrm{inc},B}\right]. \tag{74}$$

3.3 Diffuse neutron scattering experiments

3.3.1 Set-ups at DrüchaL and RITA-II

Diffuse neutron scattering measurements were performed at temperatures above the miscibility gap using a high-temperature furnace (see Fig. 8) mounted on an Eulerian cradle (Model 512.1, Huber, Rimsting, Germany). A detailed description of the high-temperature furnace is given in the thesis of Bucher [Buch99b].

Set-up procedure. In a first step, an adjustment pin mounted in the furnace was brought to the center of the Eulerian cradle using the xy table (maximal travel of ± 10 mm, integrated in the base plate) and the z motion of the ϕ axis. The center is

kept as a reference using a theodolite. Then the sample is mounted. The cylindrically shaped sample was mounted on a sample holder (4N nickel, polycrystalline) by laser welding (see Fig. 9) to achieve good thermal contact between the sample holder and the sample. To reduce scattering contributions due to the sample holder or parts of the heating device, both were covered by boron nitride. The neck (diameter 2.5 mm, height 1.5 mm, surrounded by a plate of boron nitride shielding) was chosen to reduce the χ dependence of the scattering volume resulting in a maximal variation in the scattering volume of less than 1%. On the base plate, an N-type thermocouple (Nicrosil-Nisil) is permanently installed. The sample holder is placed on the thermocouple; the thermocouple tip is positioned about 2 mm below the neck of the sample (see Fig. 9). The N-type thermocouple is calibrated using two K-type thermocouples (Chromel-Alumel) directly welded on a polycrystalline sample with
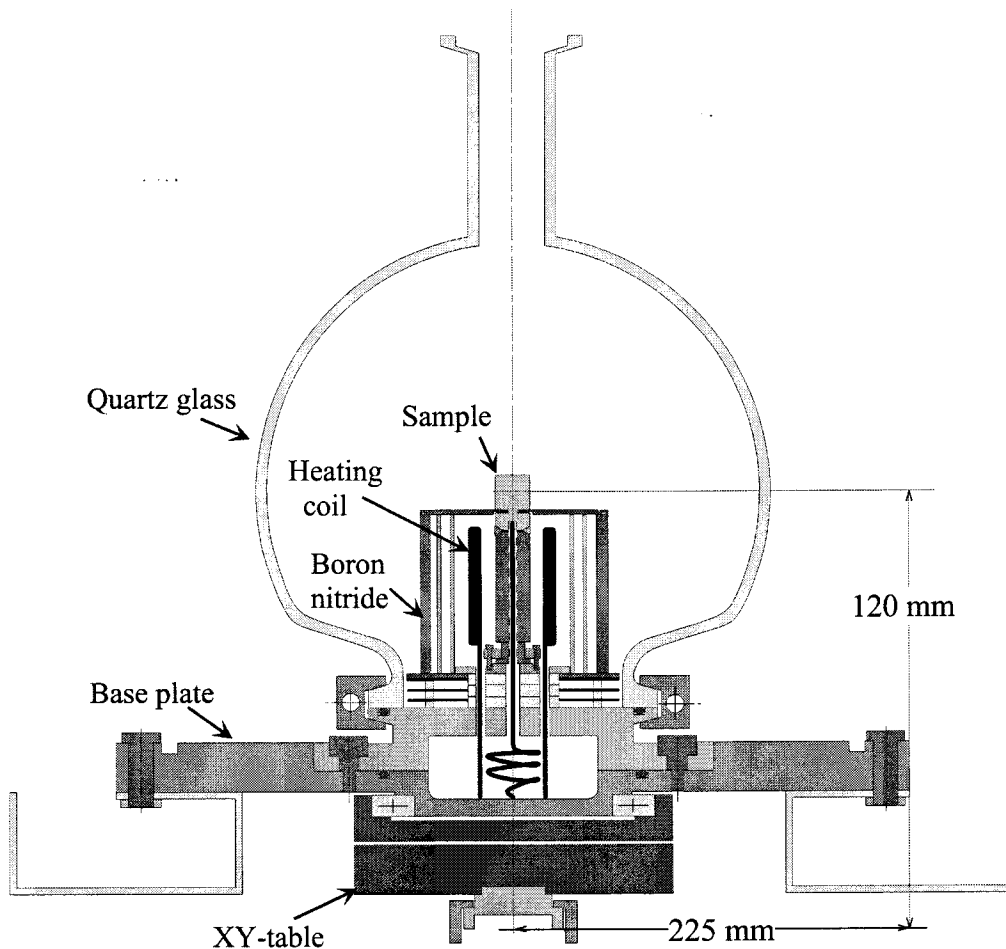

Fig. 8: Cut through the high-temperature furnace used in the diffuse scattering experiment.

similar composition and dimension as the sample used in the scattering experiment. Calibration curves for Ni-Au and Fe-Al are given in Fig. 10.

They show that the absolute value of the temperature is determined within ± 10 K (see Fig. 10 for Fe-Al above 1100 K). As the heat conduction depends on the elements used and on the diameter ratio of sample and neck, the calibration curves for Ni-rich Ni-Au and Fe-rich Fe-Al differ. In a next step, the heating device is mounted. The heating coil is made of $Mo(LaO_2)$ wired around an Al_2O_3 holder. Below 10^{-3} mbar, the $Mo(LaO_2)$ wire (diameter 0.8 mm, length ~ 2 m) is stable up to 1700 K. During a measurement, the maximal temperature variation is ± 1 K within two weeks. Two concentric heat shields (tungsten) reduce heat losses. The heating power is supplied by a power supply (PS-9072, EA, Viersen, Germany), the temperature is controlled by a Eurotherm temperature controller. Next, the orientation matrix is determined at room temperature from at least six Bragg reflections. This requires that the furnace is well rotatable around the ϕ and χ axes. At elevated temperatures, the range of χ rotation is restricted to about 60 degrees since the quartz glass cover is connected to a turbomolecular pump fixed on top of the Eulerian cradle. Therefore, the orientation matrix can only be determined from a reduced number of fundamental reflections at elevated temperatures. Heating to about 1100 K needs
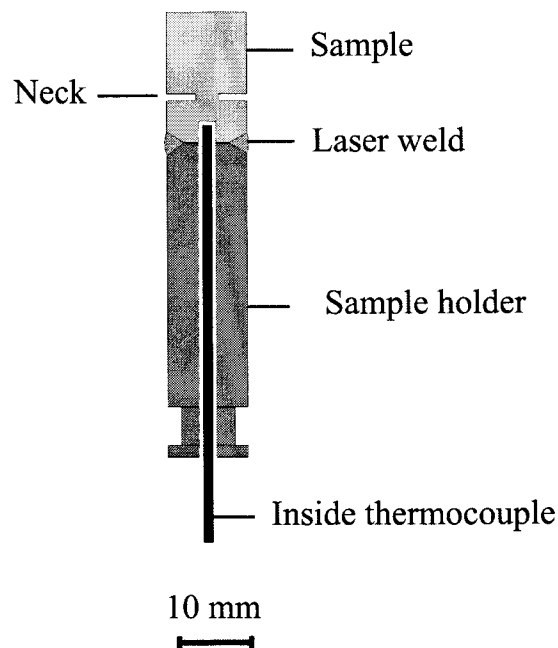

Fig. 9: ^{58}Ni-8.4 at.% Au single crystal and ^{nat}Ni sample holder. Also, the position of the thermocouple is indicated.
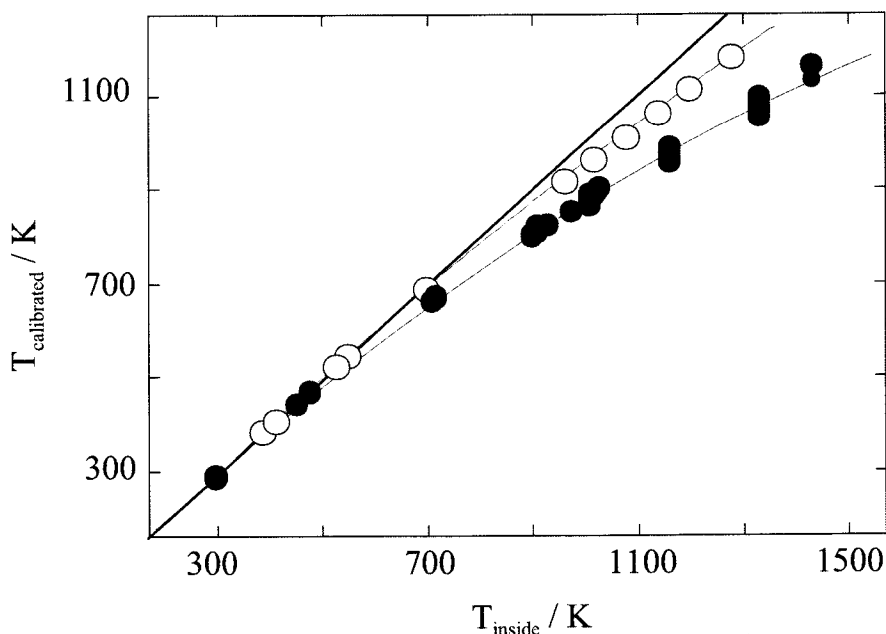
Fig. 10: Temperature calibration for Ni-8.4 at.% Au (o) and Fe-21.9 at.% Al [Buch99b] (●). The thick straight line shows equal values of the inside temperature and the calibrated sample temperature.

about three hours, the heating speed is limited by the vacuum condition required for the $Mo(LaO_2)$ wire. Cooling to about 373 K takes two hours. Finally, diffuse scattering is measured for a given set of positions in a three-dimensional volume of reciprocal space.

The triple-axis spectrometer DrüchaL. The diffuse neutron scattering of Ni-rich Ni-Au was measured on the triple-axis spectrometer (see Fig. 11) DrüchaL (PSI, Villigen, Switzerland) with an energy transfer $\Delta E = E_f - E_i$ set to nominal zero. The monochromator is composed of nine vertically focusing pyrolytic graphite single crystals having [00.2] normals. The neutron beam is focused on the sample position by tilting of the pyrolytic graphite crystals. The analyzer is composed of seven pyrolytic graphite single crystals to focus the scattered neutron beam horizontally. Slits before the sample (15 mm × 15 mm) were set in such a way that the sample is always bathed in the beam, independent of the sample tilting (χ). Slits after the sample (15 × 15 mm) and before the detector (15 mm × 160 mm) were set to reduce background scattering. No further collimation was used. The λ/n harmonics at $E_i = 14.68$ meV were suppressed by pyrolytic graphite (10.5 cm in length) [Loop66] leading to $I_{\lambda/2}/I_\lambda \le 10^{-3}$. At an energy E_i of 4.76 meV, the λ/n

harmonics were suppressed by 17.1 cm of liquid-nitrogen-cooled beryllium [Berg66]. The scattered neutrons were registered using a ^{3}He detector (gas pressure 5 bar). To take fluctuations of the intensity of the incident neutron beam into consideration, the measurements were done under monitor control.

The elastic diffuse scattering of a ^{58}Ni-8.4 at.% Au single crystal was measured at 1083 K, about 100 K above the miscibility gap using incident neutrons of 14.68(50) meV. Typically, for ^{58}Ni-8.4 at.% Au 300-3000 counts within 840 s were registered.
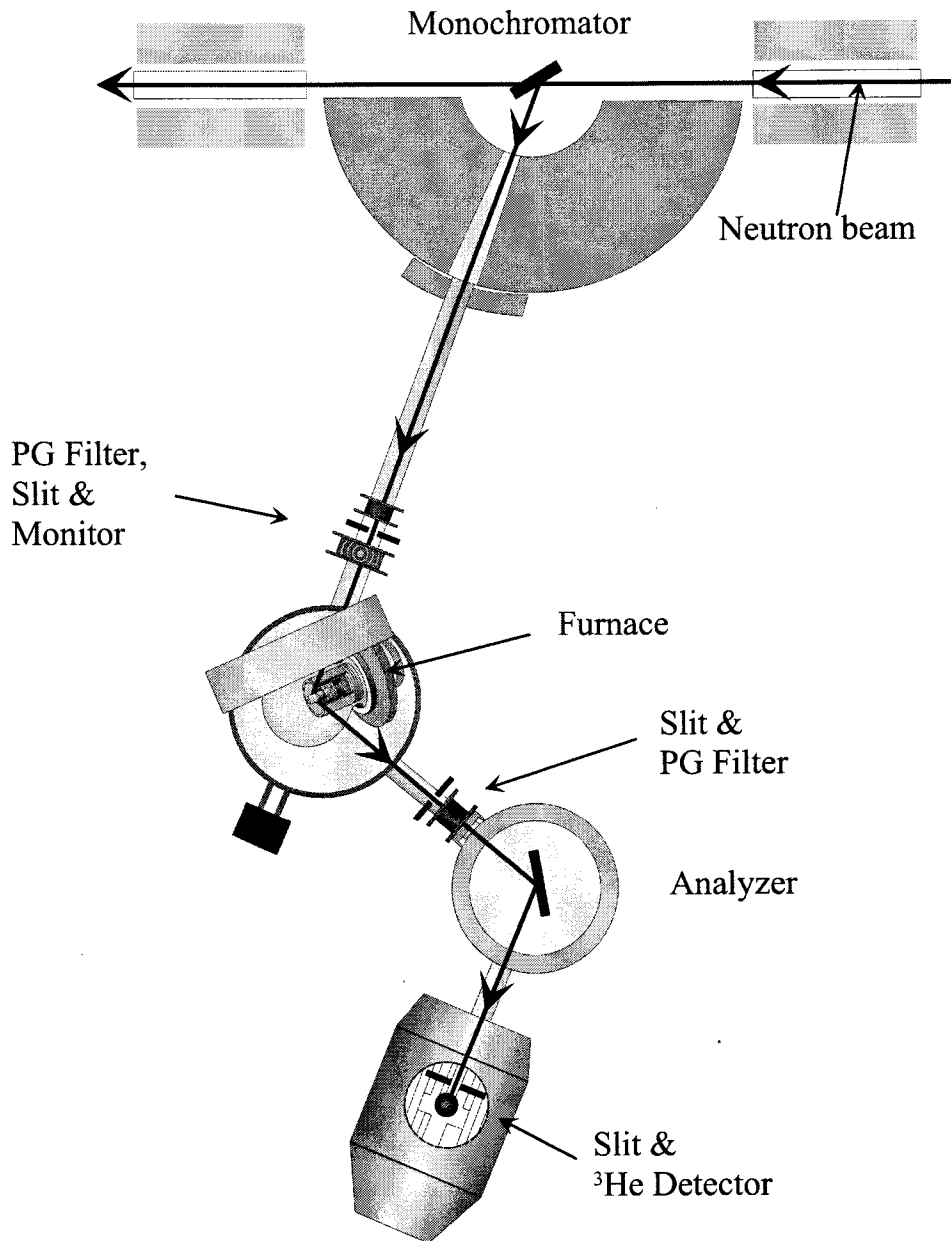

Fig. 11: Triple-axis configuration [Buch99b] used in the experiment.

The scattering intensities were measured at about 730 crystal settings located on a grid of 0.1 r.l.u. spacing within a three-dimensional volume of reciprocal space, suited for the separation of short-range order scattering and linear displacement scattering. These settings are in a scattering vector range of magnitudes from 0.2 to 2.1 r.l.u. The difference in atomic size of Ni and Au atoms is large and large displacement scattering is expected. Short-range order scattering is dominant only within the first Brillouin zone. In the case of a short-range decomposed alloy, a maximum close to 000, the origin of the reciprocal space, should be observed. To get scattering data near the origin of reciprocal space, about 20 settings along $h00$ within 0.13 to 0.60 r.l.u. were measured using neutrons of 4.76(15) meV.

To convert the diffuse scattering intensities to absolute units for both diffuse neutron scattering measurements, the elastic incoherent scattering of a vanadium sample with identical dimensions as the sample was measured. For background corrections the scattering of a cadmium sample (identical dimensions as the sample) and of the empty furnace was measured.

Measurements on the triple-axis spectrometer RITA-II. In 2001, the triple-axis spectrometer DrüchaL was replaced by the triple-axis spectrometer RITA-II. The diffuse neutron scattering of ^{58}Ni-60 at.% Au at 1023 K, about 30 K above the miscibility gap, was therefore measured on the triple-axis spectrometer RITA-II. The triple-axis spectrometer was equipped with the high-temperature furnace and an Eulerian cradle. For incident neutrons of 14.7(5) meV, pyrolytic graphite was used to suppress higher harmonics. Typically, 200-700 counts within 5400 s were registered. The scattering intensities were measured at about 20 positions along $h00$ within 0.2 to 1.8 r.l.u. At all positions the scattering of a vanadium and a cadmium sample with identical dimensions as the sample and the scattering of the empty furnace were measured.

The transmission factors of a ^{58}Ni-8.4 at.% Au, a Fe-20.6 at.% Al and a ^{58}Ni-8.4 at.% Ti single crystal were measured between 293 K and 1100 K on the triple-axis spectrometer RITA-II (PSI, Villigen, Switzerland). The incoming neutron beam ($E_i = 14.7(5)$ meV) was collimated (collimation of 40'), and the λ/n harmonics were largely eliminated using pyrolytic graphite (5.1 cm in thickness). To illuminate a well-defined scattering volume of the sample, close slits (3 mm × 5 mm) were set in front of the sample. Measuring the transmitted neutron beam of the sample and the empty configuration gives directly the transmission factor and the linear absorption coefficient of the samples.

3.3.2   Data corrections and calibration

Neutron scattering from the sample environment (e.g. quartz glass or boron nitride) gives additional scattering contributions. To avoid systematic errors due to these scattering contributions, scattering intensities were eliminated according to the following criteria.

(i) Scattering intensities in the range of the Debye-Scherrer rings of the boron nitride cover (see Fig. 12) were eliminated.

(ii) Close to fundamental reflections, the energy transfer for the excitation of acoustic phonons decreases to zero values. Therefore, thermal diffuse scattering can no longer be discriminated experimentally; for an energy resolution of 0.5 meV, scattering intensities within 0.25 r.l.u. around the fundamental reflections are affected by thermal diffuse scattering and are not considered in the evaluation.

(iii) The increase of the scattering intensities due to the sample environment near the incident beam direction is seen in Fig. 12. Therefore, scattering intensities within 0.4 r.l.u. around 000 ($E_i = 14.68$ meV) are not considered in the evaluation, for $E_i = 4.76$ meV not within 0.15 r.l.u.

The as-measured diffuse neutron scattering and the small-angle scattering of each position $\underline{Q}$ were corrected for background using eq. (67). Both, the elastic diffuse scattering of the sample and the elastic incoherent scattering of vanadium were background corrected.

The transmission factor A for cylindrically shaped samples investigated in a wide-angle scattering experiment depends on the scattering angle 2θ. For the cylindrically shaped Ni-Au and V samples it is

$$A(\theta) = e^{-[a_1 + b_1 \sin^2(\theta)]\mu r - [a_2 + b_2 \sin^2(\theta)]\mu^2 r^2} \tag{75}$$

with $a_1 = 1.7133$, $b_1 = -0.0386$, $a_2 = -0.0927$ and $b_2 = -0.3750$ as given by Rouse and coworkers [Rous70] and Hewat [Hewa79]. The linear absorption coefficient μ includes the thermal diffuse scattering calculated using eq. (58).

Parameters used in the calibration. Owing to static and dynamic atomic displacements from the average lattice, the scattering amplitudes are attenuated by an exponential factor, the Debye-Waller factor, the exponent of the Debye-Waller
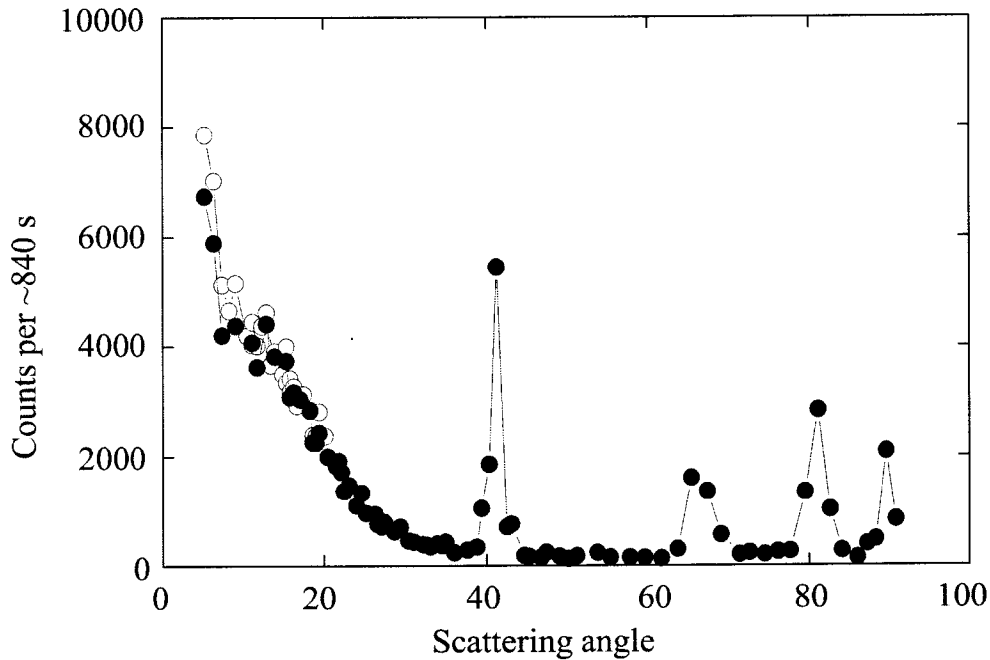
Fig. 12: Typical measurements; empty sample holder (o) and Cd sample (•).

factor being

$$2M(\underline{Q}) = 2B(\underline{Q})\frac{\sin^2(\theta)}{\lambda^2}. \tag{76}$$

Assuming that the static and dynamic atomic displacements are uncorrelated, $B(\underline{Q})$ is given as the sum of a static and a dynamic part, B_{sta} and B_{dyn}.

The static part B_{sta} was derived by Krivoglaz [Kriv96b] based on the assumption that the solute atoms in a dilute solution can be treated as point defects. For point defects with cubic symmetry in an elastic continuum, the static Debye-Waller factor is given by

$$B_{sta} = 2a_1 c_A (1 - c_A) \left(\frac{1 + \nu}{1 - \nu}\right)^2 \left(3\frac{\partial a}{\partial c_A}\right)^2, \tag{77}$$

with Poisson's number ν

$$\nu = \frac{c_{12}}{c_{12} + c_{11}} \tag{78}$$

and the constant a_1 that has a value of 0.0587 for the fcc structure. The derivative of the lattice parameter a of Ni-Au with respect to the concentration c_{Au} is taken from Okamoto [Okam87]. The elastic constants $c_{11} = 204\,\text{GPa}$, $c_{12} = 141\,\text{GPa}$ and $c_{44} = 89\,\text{GPa}$ for Ni-8.4 at.% Au at 1083 K are estimated from the elastic constants of pure Ni and Au [Simm71].

The dynamic part B_{dyn} is (Debye model see section 2.2.3)

$$B_{\text{dyn}} = \frac{11492T}{m\theta_{\text{D}}^2}\Phi(\theta_{\text{D}}/T) + \frac{2837}{m\theta_{\text{D}}} \tag{79}$$

where θ_{D} is the Debye temperature and m the average atomic mass. The values for the integral function $\Phi(\theta_{\text{D}}/T)$ are listed in [Macg62]. The Debye temperature θ_{D} is determined from the elastic constants by

$$\theta_{\text{D}} \propto J\Big(\frac{c_{44}}{c_{11} - c_{44}}, \frac{c_{12} + c_{44}}{c_{11} - c_{44}}\Big) \tag{80}$$

where the function J is determined according to Leibfried [Leib55]. For the static part B_{stat} and the dynamic part B_{dyn} values of $0.115 \times 10^{-2}\,\text{nm}^2$ and $1.481 \times 10^{-2}\,\text{nm}^2$ were obtained. For vanadium measured at room temperature $B = 0.485 \times 10^{-2}\,\text{nm}^2$ was used [Cole70].

Multiple scattering was estimated in the quasi-isotropic approximation of Vineyard [Vine54] for zero-energy transfer. The correction term D consists of one part $F(\mu, R, H)$ that depends on the scattering geometry and a second part that depends on the elastic scattering cross-sections and the absorption cross-section

$$D = F(\mu, R, H)\frac{\sigma_{\text{coh}} + \sigma_{\text{inc}} + \sigma_{\text{TDS}}}{\sigma_{\text{coh}} + \sigma_{\text{inc}} + \sigma_{\text{abs}} + \sigma_{\text{TDS}}}. \tag{81}$$

The variable R is the radius of the cylindrically shaped sample and H its height. The values of $F(\nu, R, H)$ for different geometries and linear absorption coefficients μ are listed in [Sear75].

Calibration. The corrected scattering intensities I_i^{cor} per monitor L_i of the sample (S) and the vanadium standard (V) are expressed by

$$\frac{I_i^{\text{cor}}/L_i}{\Phi\Delta\Omega\Delta E} = A_i(1 + D_i)N_i \int_0^\infty f(E_{\text{f}})\frac{d\sigma_i^2}{d\Omega dE_{\text{f}}}dE_{\text{f}}. \tag{82}$$

As the detector efficiency $f(E_{\text{f}})$ and the flux Φ can not be determined experimentally with high accuracy, the common approach is to consider them by measuring the elastic incoherent scattering of vanadium under identical conditions. Then, the differential scattering cross-section of the sample is expressed by

$$\Big(\frac{d\sigma}{d\Omega}\Big)_{\text{S}} = \frac{L_{\text{V}}}{L_{\text{S}}}\frac{A_{\text{V}}}{A_{\text{S}}}\frac{1 + D_{\text{V}}}{1 + D_{\text{S}}}\frac{I_{\text{S}}^{\text{cor}}}{I_{\text{V}}^{\text{cor}}}\frac{N_{\text{V}}}{N_{\text{S}}}\Big(\frac{d\sigma}{d\Omega}\Big)_{\text{V}}. \tag{83}$$

The elastic incoherent scattering of vanadium is given by

$$\left(\frac{d\sigma}{d\Omega}\right)_V = \frac{\sigma_{\text{inc,V}}}{4\pi}e^{-2M_V}. \tag{84}$$

Using the monotonic Laue scattering of a statistically uncorrelated atomic arrangement of the elements A and B as a reference and subtracting the elastic incoherent scattering, the elastic diffuse scattering in Laue units is

$$\left(\frac{d\sigma}{d\Omega}\right)_S^{\text{coh}} = \frac{1}{c_A c_B \mid b_A - b_B \mid^2}\left[\frac{L_V}{L_S}\frac{A_V}{A_S}\frac{1 + D_V}{1 + D_S}\frac{I_S^{\text{cor}}}{I_V^{\text{cor}}}\frac{e^{-2M_V}}{e^{-2M_S}}\frac{N_V}{N_S}\frac{\sigma_{\text{inc,V}}}{4\pi}\right.$$
$$\left. - c_A\sigma_{\text{inc,A}} + c_B\sigma_{\text{inc,B}}\right] \tag{85}$$

consisting of short-range order scattering and displacement scattering. For the total error, the counting statistics have to be considered. Thus, large incoherent elastic scattering results in large error bars. Since the incoherent elastic scattering was strongly reduced using the Ni-58 isotope (see Table 2), the errors decreased considerably.

4 Results

Aspects such as the optimization of the scattering contrast, a previously proposed correction procedure for α_{000} [Port02] and the transmission factor measured at elevated temperatures are introduced first. These aspects are considered in the data correction and the calibration for the small-angle neutron scattering data of [58]Ni-8.3 at.% Au and the diffuse neutron scattering data of [58]Ni-8.4 at.% Au. The local atomic arrangement of [58]Ni-8.4 at.% Au is subsequently characterized by a configurational analysis of model crystals, and effective pair interaction parameters are determined.

4.1   Optimization of scattering contrast

The elastic neutron scattering cross-section of natural nickel in the region between the fundamental reflections is dominated by the elastic incoherent scattering. In order to increase the elastic coherent scattering and to decrease the elastic incoherent scattering of nickel, the Ni-58 isotope was used in the sample preparation instead of natural Ni.

In Fig. 13 the elastic diffuse neutron scattering of two Ni-rich Ni-Au single crystals measured at 1083 K is shown. Both single crystals had comparable composition, but different isotopic contents. Large differences are observed in the diffuse scattering as the incoherent elastic scattering of natural Ni and [58]Ni differ largely. For

Table 2: Elastic coherent and incoherent scattering cross-sections and the absorption cross-section for [nat]Ni-10 at.% Au and [58]Ni-8.4 at.% Au calculated for a wavelength of 2.361 Å.

Composition	σ_{coh} [barn]	σ_{inc} [barn]	σ_{abs} [barn]
[nat]Ni-10.0(4) at.% Au	0.081(6)	4.723(422)	18.4(25)
[58]Ni-8.4(4) at.% Au	0.441(32)	0.036(6)	16.4(23)
Expressions in appendix D.			
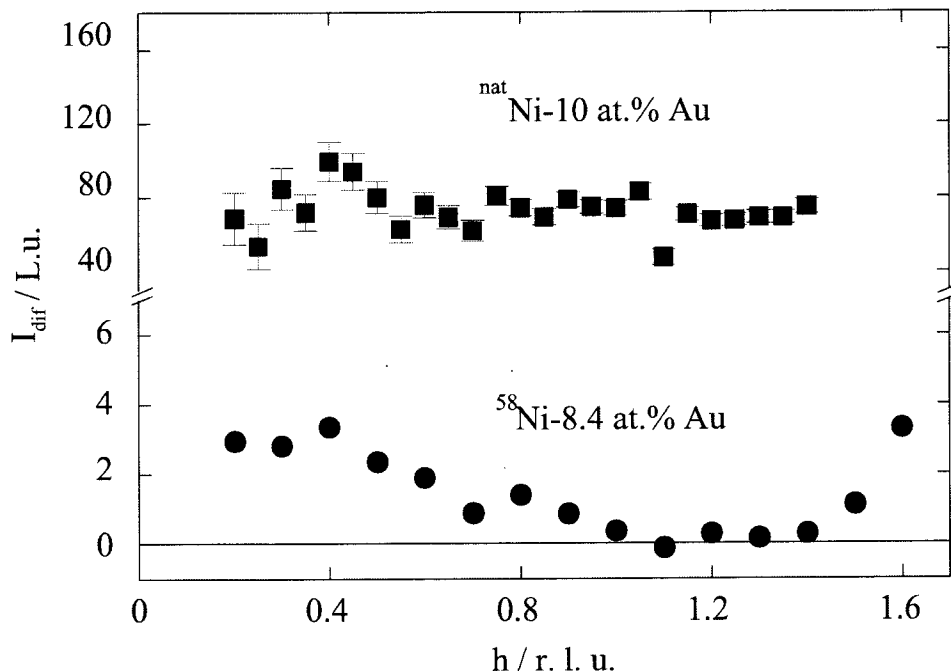
Fig. 13: Coherent and incoherent elastic diffuse scattering (in Laue units) measured at 1083 K of two Ni-rich Ni-Au single crystals that have similar composition, but different isotopic contents.

^{58}Ni-8.4 at.% Au it is only 10% of the elastic diffuse scattering and consequently, the modulations due to short-range order scattering and displacement scattering can be unambiguously identified. From the isotopic replacement, the coherent scattering contrast benefits as well (not visible in a Laue unit representation of the short-range order scattering). It increases by about a factor of 6.4 (see Table 2). Without isotopic replacement, the elastic coherent scattering contributions of Ni-rich Ni-Au alloys cannot be determined, as the elastic incoherent scattering dominates (98% of the elastic diffuse scattering).

4.2 Earlier evaluation

The calibrated elastic diffuse scattering from ^{58}Ni-8.4 at.% Au determined in an earlier evaluation [Port02] is shown in Fig. 14. A maximum in diffuse scattering is found at 000. No sign of a static concentration wave along $\langle 100 \rangle$ is noticeable between the fundamental reflections, in contrast to predictions by Wolverton and coworkers [Wolv97] for Ni-25 at.% Au. From the calibrated scattering intensities, short-range order parameters α_{lmn} and atomic displacements γ_{lmn}^{x}, δ_{lmn}^{x} and ϵ_{lmn}^{xy}
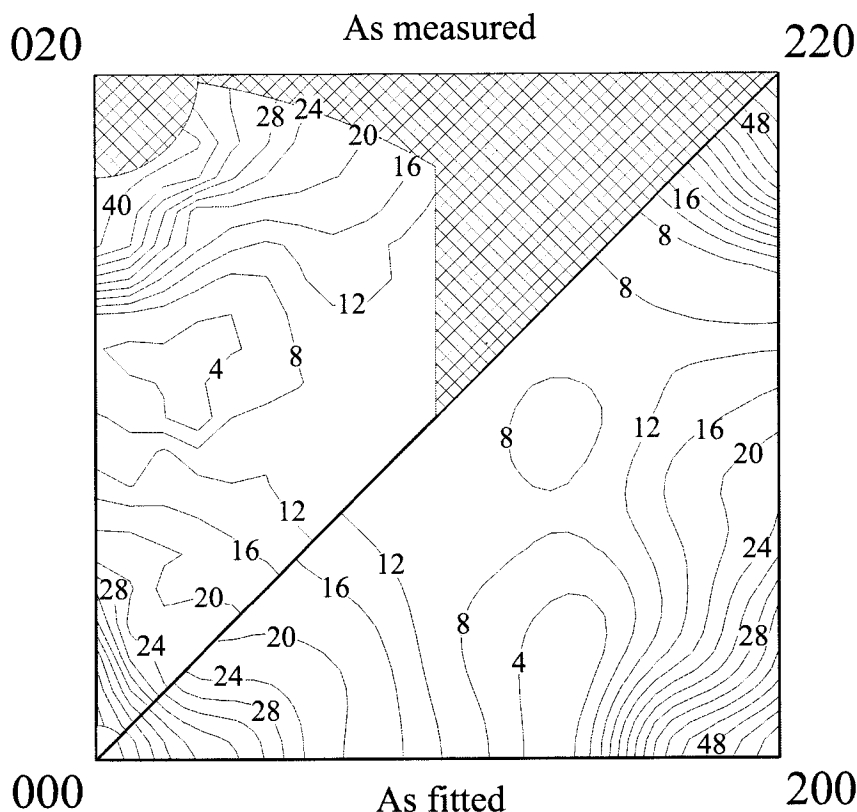
Fig. 14: The as-measured and recalculated elastic diffuse scattering (in 0.1 Laue units, no correction for α_{000}) from ^{58}Ni-8.4 at.% Au at h_1h_20 positions.

were determined using the least-squares fitting procedure given by Williams [Will72] (see appendix E). The quality of each fit was judged from its weighted R value and χ^2. To stabilize the least-squares fitting, the scattering intensity at 000 was set equal to that at 0.13 0 0. Finally, a set of 13 parameters α_{lmn} (see Table 5), 33 γ_{lmn}^x and 9 $\delta_{lmn}^x/\epsilon_{lmn}^{xy}$ were used. The recalculated elastic diffuse scattering (see Fig. 14) reproduces the experimental data within ± 0.2 L. u., well within the standard deviation of 0.3 L. u. solely due to counting statistics.

As expected, in this first evaluation, a value of 0.59(4) was found for α_{000}, much smaller than the theoretical value of one. Based on a procedure developed for correcting the short-range order parameters of Fe-21.9 at.% Al (where the same problem with α_{000} was encountered), a multiplicative factor and an additive term were determined, each correcting for half of the deviation of α_{000} from one. The same correction procedure was applied for Ni-Au and resulted in a multiplicative

factor of 1.2 and an additive term of 0.2 Laue units [Port02]. In the least-squares fitting a set of 17 α_{lmn}, 18 γ_{lmn}^x and 8 $\delta_{lmn}^x/\epsilon_{lmn}^{xy}$ was determined. The value of α_{000} was 0.97(4). This first correction procedure is referred to as *earlier evaluation*.

4.3   Transmission factors

The transmission factor of ^{58}Ni-8.4 at.% Au depends significantly on temperature (see Fig. 15). Similar results are obtained for ^{58}Ni-9.6 at.% Ti and Fe-21.9 at.% Al. For ^{58}Ni-8.4 at.% Au and ^{58}Ni-9.6 at.% Ti a decrease of 22(4)% was observed, for Fe-21.9 at.% Al a decrease of 15(3)%. These results indicate, that the linear absorption coefficient increases with increasing temperature, since the thermal diffuse scattering cross-section increases. The thermal diffuse scattering cross-section σ_{TDS} was therefore calculated using eq. (58). Subsequently calculated transmission factors for ^{58}Ni-8.4 at.% Au and ^{58}Ni-9.6 at.% Ti (scaled to the experimental values at room temperature) are in good agreement with the measured transmission factors (see Fig. 15). These findings show that the thermal diffuse scattering has to
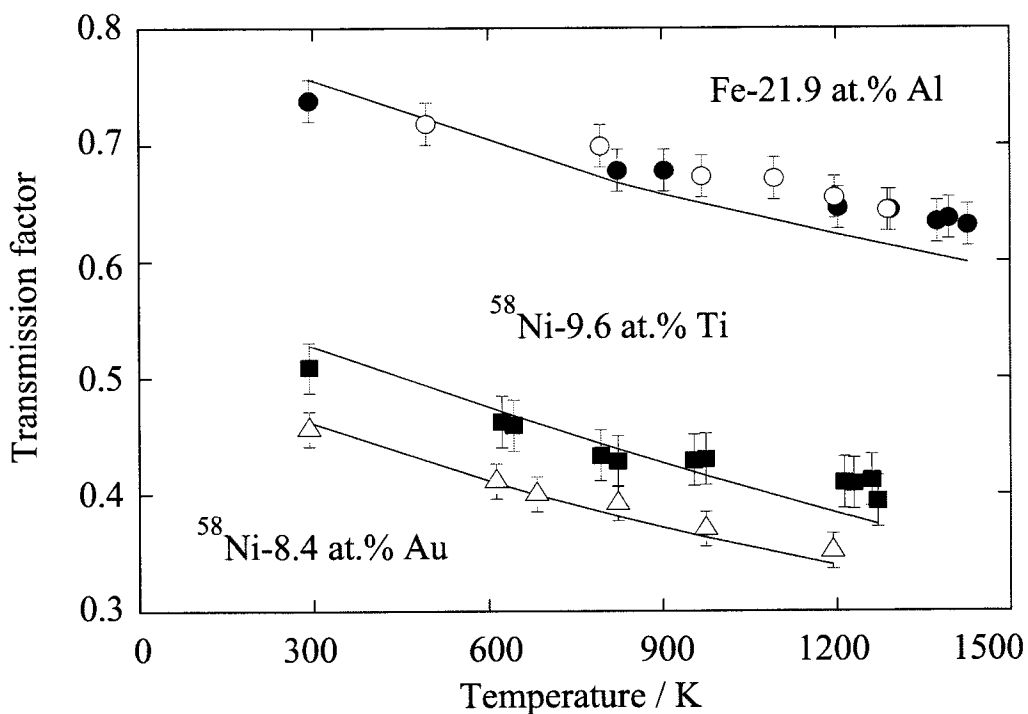

Fig. 15: Transmission factors of Fe-21.9 at.% Al, ^{58}Ni-8.4 at.% Au and ^{58}Ni-9.6 at.% Ti. The solid lines are recalculated transmission factors (scaled to the experimental value at room temperature) according to eq. (68) and (75).
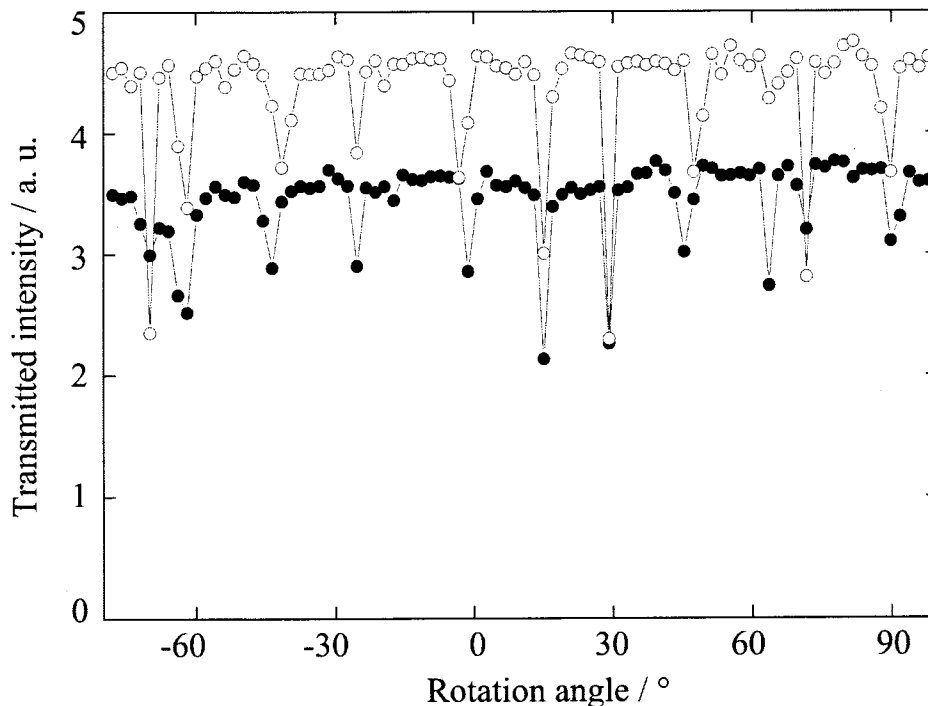
Fig. 16: Transmitted intensity of a ^{58}Ni-8.4 at.% Au single crystal within a rotation angle range of 180° at (o) room temperature and (•) 1083 K.

be taken into consideration explicitly in the data correction and the calibration of diffuse neutron scattering data.

When rotating the ^{58}Ni-8.4 at.% Au sample, a large number of small dips in the transmitted intensity (width ~2°) were observed (see Fig. 16), attributed to the excitation of fundamental reflections. The presence of the dips indicates that in principle, the transmission factor has to be measured at each position where the diffuse scattering is measured. The variation in the intensity of the transmitted neutrons between the dips with temperature shows that the variation in the transmission factors is large.

Estimate of the effect on α_{000}. For the cylindrically shaped Ni-Au, Ni-Ti and Fe-Al samples, the linear absorption coefficient μ and the transmission factor $A(\theta = 0)$ were calculated at 0 K and at sample temperature, using eq. (68) and (75). The ratio of these transmission factors is given in Table 3. The Debye temperatures of Fe-21.9 at.% Al, ^{58}Ni-8.4 at.% Au, ^{58}Ni-9.6 at.% Ti and ^{58}Ni-5.8 at.% Ti were calculated according to Leibfried [Leib55] on the basis of elastic constants and are all between 300 to 400 K. At elevated temperatures, the ratio of the transmission factors is 0.7(1) for the Ni-Au and Ni-Ti alloys, smaller than for Fe-Al owing to the larger

Table 3: The calculated total thermal diffuse scattering cross-section σ_{TDS} and the ratio of the transmission factors of Ni-Ti, Ni-Au, Fe-Al and V at 0 K and sample temperature T.

	T [K]	θ_D [K]	λ [Å]	σ_{TDS} [barn]	diameter [mm]	ratio
Alloys						
[58]Ni-5.8 at.% Ti	293	451.0	2.361	1.39(2)	9.0	0.910(2)
[58]Ni-9.6 at.% Ti	1103	381.9	2.361	5.39(8)	9.0	0.704(7)
[58]Ni-8.4 at.% Au	293	341.7	2.361	1.38(3)	8.0	0.920(2)
	1083		2.361	6.64(12)	8.0	0.690(10)
Fe-21.9 at.% Al	293	324.4	2.361	0.82(1)	10.0	0.949(1)
	878		2.361	3.08(5)	10.0	0.821(4)
	966		2.361	3.43(5)	10.0	0.803(4)
	1073		2.361	3.85(6)	10.0	0.782(5)
Pure metal						
V	293	380.0	2.361	0.323(4)	8.0	0.9841(3)

scattering cross-sections σ_{coh} and σ_{inc}. For Ni-Au, the elastic coherent scattering and α_{000} are expected to increase by at least 30% as the influence of thermal diffuse scattering for vanadium measured at room temperature is negligible.

4.4   Small-angle neutron scattering

The small-angle scattering of the as-quenched [58]Ni-8.3 at.% Au polycrystal was first measured at room temperature and then at 1173 K to check the quality of the quenching. For both data sets the data correction and the calibration were performed considering explicitly the thermal diffuse scattering calculated according to Kothari and Singwi [Koth59]. Since the average grain size was smaller than the sample size and the scattering pattern corresponds to an average of scattering patterns over many grain orientations, isotropic scattering patterns were observed and the calibrated scattering data were azimuthally averaged. Within the solid solution, no stable long-range density fluctuation is present, and a flat scattering pattern is expected in the scattering vector range 0.05 to 0.14 r.l.u., of the same order at 293 K (as-quenched) and at 1173 K. For small-angle scattering measured within the miscibility gap, a significant increase in scattering intensity near the incoming beam is expected owing to Au-rich precipitates within a Ni-rich matrix.
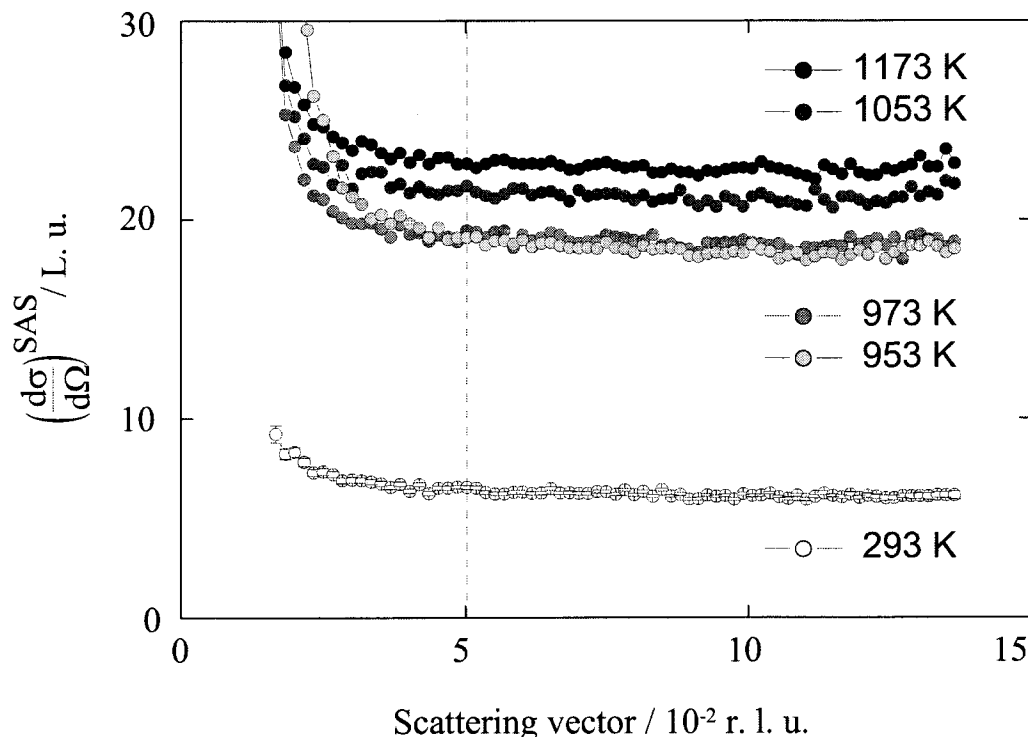
Fig. 17: The azimuthally-averaged small-angle scattering of a [58]Ni-8.3 at.% Au polycrystal registered at 293 (as-quenched), 953, 973, 1053 and 1173 K.

The scattering curves measured at 293 K (as-quenched state) and at 1173 K differ by a large constant scattering contribution of 16.4(4) L. u. in the scattering vector range 0.05 to 0.14 r. l. u. (see Fig. 17). Near the incident beam direction, the scattering intensities increase for the as-quenched state, indicating that decomposition in the scattering vector range 0.05 to 0.14 r. l. u. was not entirely suppressed by the quench. An increase in small-angle scattering intensities was observed at elevated temperatures (probably due to small-angle scattering on Au decorated grain boundaries). At 953 K, 20 K below the phase boundary of the miscibility gap, an additional increase in small-angle scattering intensity was measured (after 600 s), indicating that Au-rich precipitates within the Ni-rich matrix are present.

Small-angle scattering patterns measured between 953 K and 1173 K revealed a systematic increase in intensity with increasing temperature. This large increase is rather unexpected, but was also observed (to a smaller extent) for the [58]Ni-60 at.% Au polycrystals. Since in cooling curves for both alloys the scattering intensity (within 0.05 to 0.14 r. l. u.) depends approximately linear on temperature, thermal diffuse scattering was used to explain this increase in the scattering intensity.

Table 4: Summary of the calculated thermal diffuse scattering [eq. (58)], the azimuthally-averaged small-angle scattering (average value over 57 scattering intensities within 0.04 to 0.14 r. l. u.) and the difference of these two scattering contributions for ^{58}Ni-8.3 at.% Au. The error bar corresponds to the standard deviation.

T	$\left(\frac{d\sigma}{d\Omega}\right)^{\text{TDS}}$	$\left(\frac{d\sigma}{d\Omega}\right)^{\text{SANS}}$	$\left(\frac{d\sigma}{d\Omega}\right)^{\text{dif}}$
[K]	[L. u.]	[L. u.]	[L. u.]
1173	17.1(4)	22.6(3)	5.5(5)
1143	16.7(4)	22.4(3)	5.7(5)
1113	16.2(4)	21.8(3)	5.6(5)
1083	15.7(4)	22.0(3)	6.3(5)
1053	15.2(4)	21.2(3)	6.0(5)
1023	14.7(4)	20.0(3)	5.3(5)
993	14.2(4)	19.3(3)	5.1(5)
973	13.9(4)	18.9(3)	5.0(5)
953	13.6(4)	18.5(3)	4.9(5)
293	3.1(3)	6.2(2)	3.1(4)

Thermal diffuse scattering. One argument why at small scattering angles no thermal diffuse scattering is observed, is that the coherent one-phonon scattering depends on the square of the scattering vector Q and is thus negligibly small. This argument is correct as long as only normal processes are considered. Inelastically scattered neutrons (mainly due to phonon absorption) registered within an energy window covering energy transfers between 0 and 60 meV, for example, can be attributed to scattering vectors up to about 2 reciprocal lattice units (r. l. u.). Since in this case large scattering vectors Q are provided, one-phonon scattering as described by Umklapp processes [Kitt76] is present.

Using eq. (58), the thermal diffuse scattering was estimated for vanadium and ^{58}Ni-8.3 at.% Au [Koth59]. For vanadium at room temperature σ_{TDS} is 0.3(2) barn and the transmission factor A is 0.77(1) (at $\lambda = 8$ Å); at 1173 K, σ_{TDS} is 1.97(12) barn and $A = 0.74(1)$. For a (standard) calibration with vanadium at room temperature, σ_{TDS} is much less than σ_{inc} and σ_{abs} (see Table 11) and is of no significance. For ^{58}Ni-8.3 at.% Au, however, the thermal diffuse scattering at elevated temperatures is important in the calculation of the transmission factor.

Between room temperature and 1173 K, the calculated thermal diffuse scattering contribution increases by about 14 L. u. (see Table 4). The difference between the as-measured and calculated scattering contributions is attributed to elastic diffuse

scattering $(d\sigma/d\Omega)^{\text{dif}}$, having a maximal value of 6.3(3) L. u. at 1083 K. If the as-quenched state corresponded exactly to the solid solution at 1173 K, the elastic diffuse scattering would be the same for both cases. This is not observed, as only a value of 3.1(2) L. u. instead of 5.5(3) L. u. was determined for the as-quenched state. Whether this is a consequence of insufficient quenching or an incomplete description of the thermal diffuse scattering contribution needs further investigation.

4.5 Diffuse neutron scattering

4.5.1 Measurements at two wavelengths

The calibrated elastic diffuse neutron scattering measured with two energies E_i is shown in Fig. 18. Both data sets show a smooth overlap and are treated as one data set. Taking the thermal diffuse scattering into consideration in the data correction and the calibration led to a nearly perfect overlap.
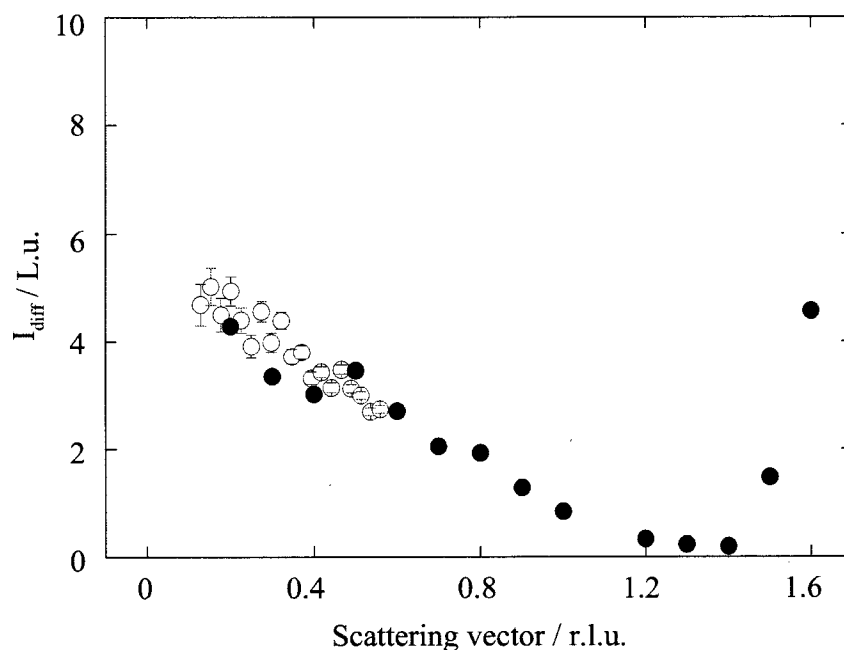
Fig. 18: Elastic diffuse scattering (in Laue units) of ^{58}Ni-8.4 at.% Au measured at 1083 K using an incident neutron energy E_i of 4.76(15) meV (o) and 14.68(50) meV (•).

4.5.2 Short-range order scattering

If one considers the correct value of the linear absorption coefficient (with respect to uncorrected data), the value of D changes from 0.0109 to 0.155 and the transmission factor $A(\theta = 0)$ from 0.39 to 0.27. A set of 19 α_{lmn}, 23 γ^x_{lmn} and 10 $\delta^x_{lmn}/\epsilon^{xy}_{lmn}$ was determined using the least-squares fitting [Will72]. For α_{000} a value of 0.99(4) was found (see Table 5). The short-range order parameters are in close agreement with those determined in the earlier evaluation [Port02], the sequence in signs is identical. The maximal scattering intensity extrapolated versus the incoming beam is 5.0(3) L. u., slightly underestimating the value of 6.3(3) determined in the small-angle neutron scattering experiment.

The dominant Fourier coefficient α_{110} is positive as expected for a decomposing alloy. The subsequent α_{lmn} are mostly positive. They approach zero smoothly and rapidly. The recalculated short-range order scattering patterns (see Fig. 19) are very

Fig. 19: Short-range order scattering I_{SRO} (in 0.1 Laue units) of ^{58}Ni-8.4 at.% Au (based on corrected scattering intensities) at h_1h_20 positions.

Table 5: Warren-Cowley short-range order parameters α_{lmn} of ^{58}Ni-8.4 at.% Au at 1083 K: uncorrected, this work and earlier evaluation [Port02]. The numbers in parentheses are the standard deviations due to counting statistics.
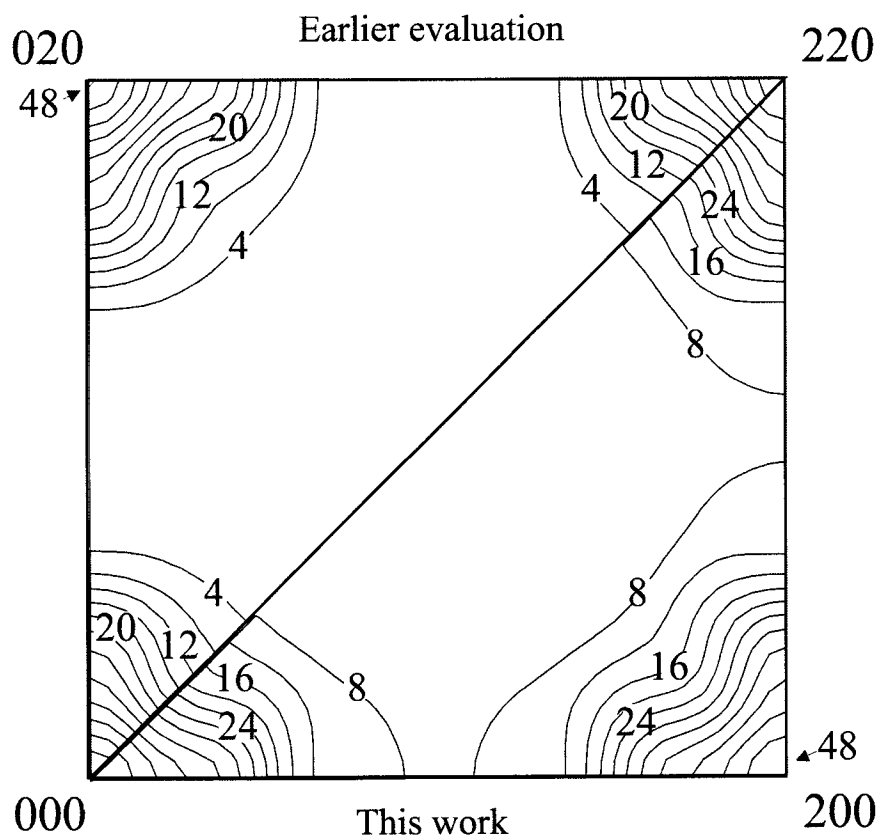
		α_{lmn}	
lmn	uncorrected	this work	earlier evaluation
000	0.594(29)	0.992(42)	0.970(41)
110	0.133(11)	0.197(14)	0.174(10)
200	0.084(10)	0.122(16)	0.099(13)
211	0.015(6)	0.016(8)	0.034(6)
220	0.008(4)	0.001(6)	0.013(4)
310	0.021(4)	0.017(5)	0.023(4)
222	–0.007(4)	–0.012(6)	–0.008(5)
321	0.000(2)	–0.003(3)	–0.001(2)
400	0.013(4)	0.017(6)	0.020(6)
330	–0.001(3)	–0.002(4)	–0.003(4)
411	0.009(2)	0.012(3)	0.017(3)
420	0.006(2)	0.005(3)	0.011(3)
233	–0.004(2)	–0.007(3)	–0.011(3)
422		–0.000(3)	–0.003(3)
431		–0.003(2)	–0.003(2)
510		0.010(3)	0.016(3)
521			0.004(2)
R	0.516	0.131	0.132
χ^2	11.5	13.7	0.333

similar, but are different concerning the absolute height in the region between the maxima. Both short-range order scattering patterns do not show maxima in the region between the fundamental reflections, in contrast to predictions of Wolverton and coworkers [Wolv97] or Wu and Cohen [Wu83].

4.5.3 Linear displacement scattering

The linear displacement parameters γ^x_{lmn} are summarized in Table 6 and agree with those determined in the earlier evaluation within the statistical error bar. In the linear displacement scattering (see Fig. 20), large modulations due to the large atomic size mismatch of 15% between Ni and Au are observed. For both methods, the scattering patterns look alike, but they differ in the values of the minima (by about 0.4 L.u.). The linear displacement scattering is antisymmetric around the

Table 6: Linear displacement parameters γ^x_{lmn} of ^{58}Ni-8.4 at.% Au at 1083 K. The numbers in parentheses are the standard deviations due to counting statistics.

lmn	this work γ^x_{lmn}	earlier evaluation γ^x_{lmn}
110	0.198(6)	0.182(10)
200	−0.070(14)	−0.081(11)
211	−0.022(6)	−0.021(6)
121	−0.020(4)	−0.011(3)
220	−0.009(5)	−0.012(5)
310	−0.019(5)	−0.022(6)
130	−0.029(5)	−0.017(5)
222	−0.011(4)	−0.008(4)
321	0.003(4)	0.001(4)
231	−0.015(4)	−0.005(4)
123	−0.008(3)	−0.002(3)
400	−0.001(8)	−0.010(10)
330	0.001(4)	0.003(4)
411	0.004(4)	−0.003(5)
141	−0.002(2)	0.000(3)
420	0.005(3)	−0.006(4)
240	−0.004(4)	0.001(4)
233	0.008(4)	0.010(4)
422	−0.007(3)	
242	0.001(3)	
431	−0.006(2)	
341	0.007(3)	
134	−0.010(2)	

fundamental reflections with a large negative contribution at the side of smaller $|\underline{h}|$ values. Such an intensity distribution is expected if the atom with the smaller coherent scattering length (Au) has the larger atomic size.

4.5.4   Quadratic displacement scattering

The sequence of signs for the quadratic displacement parameters δ^x_{lmn} and ϵ^{xy}_{lmn} determined in this work and the earlier evaluation is identical, the values agree within the error bars (see Table 7). The recalculated quadratic displacement scattering (see Fig. 21) is strongly modulated. In both scattering patterns the maxima in the quadratic displacement scattering are located close to the fundamental reflections,
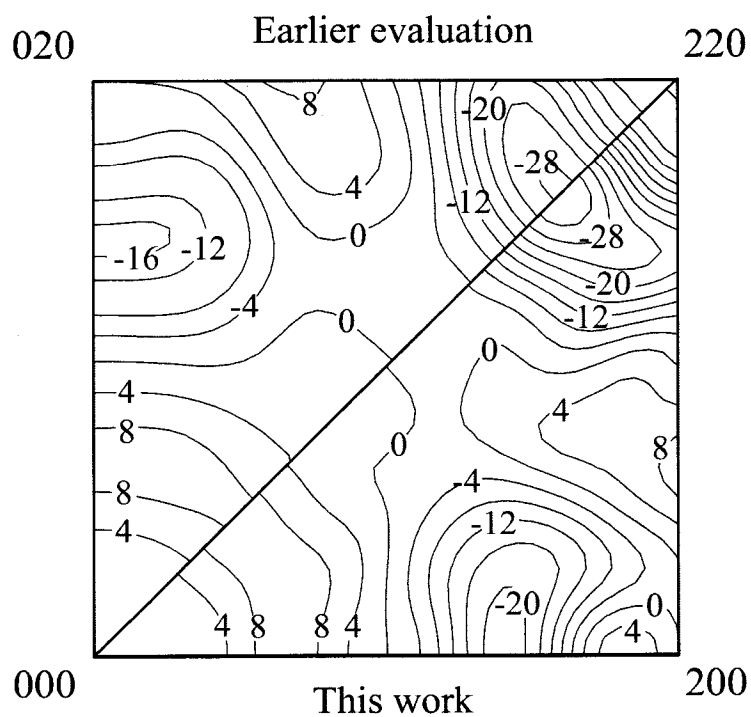
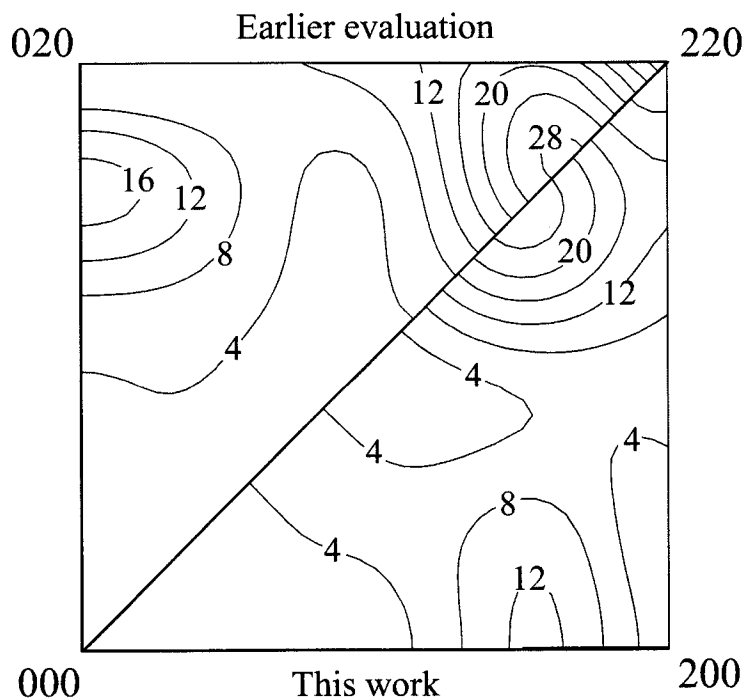Fig. 20: Linear displacement scattering I_{SE} (in 0.1 L. u.) of ^{58}Ni-8.4 at.% Au at $h_1 h_2 0$ positions.

Fig. 21: Quadratic displacement scattering I_H (in 0.1 Laue units) of ^{58}Ni-8.4 at.% Au at $h_1 h_2 0$ positions.

Table 7: The quadratic (δ^x_{lmn} and ϵ^{xy}_{lmn}) displacement parameters of ^{58}Ni-8.4 at.% Au at 1083 K determined in this work and in the earlier evaluation. The numbers in parentheses are the standard deviations due to counting statistics.

	this work		earlier evaluation	
lmn	δ^x_{lmn}	ϵ^{xy}_{lmn}	δ^x_{lmn}	ϵ^{xy}_{lmn}
000	0.327(20)		0.326(21)	
110	-0.037(6)	-0.077(10)	-0.035(5)	-0.062(11)
011	0.029(9)		0.054(7)	
200	-0.052(10)		-0.051(11)	
020	-0.023(10)		-0.009(7)	
211	-0.011(5)	0.016(8)	-0.022(5)	
121	0.011(4)	-0.002(7)	0.004(3)	

but the position of the (local) maxima are slightly shifted in radial direction. As the minima in the linear displacement scattering and the maxima in the quadratic displacement scattering are nearly at identical positions, the average magnitude of the total displacement is the same for both methods.

4.6   Configurational analysis

Based on the short-range order parameters (see Table 5) crystals were modeled. The α_{lmn} calculated for the modeled crystals lie within the statistical error bars of the experimental data. The difference between a statistically uncorrelated arrangement and a short-range decomposed model crystal is illustrated in Fig. 4 (section 2). Small groups of minority atoms (Au) on {111} planes are typical for the short-range decomposed state.

For a quantitative analysis, all nearest-neighbor configurations (Clapp configurations; for the nomenclature, see Clapp [Clap71]) were searched. Enhancement factors and abundances were obtained by averaging over five short-range decomposed and five random crystals (see Table 8). Especially, two cases were considered:

(i) The possible superstructures $L1_2$ and $L1_0$ [Zhao99] are characterized by the configurations C16, choosing the cases of minority atoms (Au) around any majority atom (Ni) for $L1_2$ and minority atoms (Au) around any minority atom (Au) for $L1_0$. As Ni-8.4 at.% Au will not yield stoichiometric ordered

structures, minority atoms must be replaced by majority atoms. This gives the sequences C16 $\to$ C7 $\to$ C3, C4. As in the evaluation, all the characteristic configurations of $L1_2$ have enhancement factors around 1 or less than 1, $L1_2$ is no plausible superstructure. On the other hand, enhancement factors larger than one are found for the characteristic configurations of $L1_0$. It is noted that Zhao and Notis [Zhao99] also found $L1_0$ as a plausible superstructure of a metastable state. The values of the enhancement factors and abundances obtained in the earlier evaluation are in close agreement with those of this work.

(*ii*) For the characterization of Au agglomerates, only the configurations of minority atoms around minority atoms with abundances larger than 2% and largest enhancement factors are summarized in Table 8. The most important configuration, C33, is a tetrahedron (C15) plus an adjacent atom as indicated by the Au agglomerates on {111} planes in Fig. 4.

Table 8: Abundances and enhancement factors of ^{58}Ni-8.4 at.% Au at 1083 K for selected Clapp configurations (considering Au around Ni for the $L1_2$ structure, Au around Au for the $L1_0$ structure and for decomposition) with respect to a statistically uncorrelated arrangement.

Clapp configuration	this work Enhancement factor	Abundance in %	earlier evaluation Enhancement factor	Abundance in %
Au around Ni				
C16	1.3	0.01	0.7	0.01
C7	0.5	0.14	0.4	0.12
C3/C4	0.5	2.42	0.4	2.25
Au around Au				
C16	16.0	0.2	5.0	0.05
C7	2.8	0.9	1.9	0.57
C3/C4	1.0	4.9	1.1	4.71
Au around Au				
C33	97.8	8.0	96.1	5.2
C31	30.3	2.2	32.2	2.6
C15	14.3	3.8	15.5	2.8
C13	14.9	8.1	9.1	5.8
C14	4.6	3.0	6.2	3.6

4.7 Effective pair interaction parameters

From the sets of α_{lmn} of Table 5, effective pair interaction parameters V_{lmn} were determined by the inverse Monte Carlo method [Gero87]. They were deduced from 200000 virtual exchanges of modeled short-range decomposed crystals with $32 \times 32 \times 32$ fcc unit cells employing linear boundary conditions. The V_{lmn} were subsequently used in Monte Carlo simulations to recalculate the Warren-Cowley short-range order parameters α_{lmn}^{rec}. For both data sets (this work and the earlier evaluation), seven V_{lmn} values are required as judged from the value of $R_\alpha = \sum_{lmn} | \alpha_{lmn} - \alpha_{lmn}^{rec} | / \sum_{lmn} | \alpha_{lmn} |$. The values and standard deviations given in Table 9 refer to five model crystals. The V_{lmn} values for the first two shells of neighbors are negative as expected for a decomposing alloy system. From the standard deviation (based on the statistical error of the α_{lmn}), just the first four parameters V_{lmn} are significant. In comparison, the effective pair interaction parameters of Ni-60 at.% Au are also given in Table 9. They were determined from a set of calculated short-range order parameters α_{lmn}, kindly provided by C. Wolverton. Only the nearest-neighbor parameter is significantly different, the next three parameters are similar to those obtained in this work.

No local minimum in $V(\underline{k}) = \sum_{lmn} V_{lmn} e^{i\underline{k}\cdot\underline{r}_{lmn}}$ is seen at the 100 position. Its presence would corroborate the metastable $L1_0$ structure found in [Zhao99], following the reasoning of Reinhard and Turchi [Rein94]. These authors interpreted a local minimum in $V(\underline{k})$ of TiV as an indicator for transient ordering in the low-

Table 9: Effective pair interaction parameters V_{lmn} of Ni-8.4 at.% Au as obtained by the inverse Monte Carlo method using the α_{lmn} of Table 5. For comparison, effective pair interaction parameters of Ni-60 at.% Au were calculated using the short-range order parameters of Wolverton and coworkers [Wolv98].

	V_{lmn} [meV] Ni-8.4 at.% Au			V_{lmn} [meV] Ni-60 at.% Au
lmn	this work	earlier evaluation	lmn	Ref. [Wolv98]
110	-48.7(97)	-37.9(60)	110	8.6
200	-46.2(163)	-19.4(79)	200	-32.9
211	19.3(94)	4.7(33)	211	5.1
220	18.4(161)	8.0(47)	220	12.3
310	3.6(36)	0.2(32)	310	-3.3
222	-6.4(67)	3.2(31)	222	2.1
321	-3.5(42)	1.4(24)	321	0.2

temperature region. Thus, no transient ordered state is indicated for ^{58}Ni-8.4 at.% Au on the basis of a local minimum in $V(\underline{k})$.

4.8 Diffuse neutron scattering of a more concentrated Ni-Au alloy

The calibrated elastic diffuse scattering from ^{58}Ni-60 at.% Au is shown in Fig. 22. A maximum in diffuse scattering is found at 000. No sign of a static concentration wave along h00 is noticeable between the fundamental reflections as found by Wu and Cohen [Wu83] (the presence of a local maximum at 0.4 r.l.u. from the wide-angle scattering data alone is not considered compulsory owing to the large errors near the incident beam). Small-angle scattering intensities measured at 1023 K agree with the elastic diffuse scattering and show a smooth overlap with the elastic diffuse scattering intensities.

At larger scattering vectors, a minimum in the diffuse scattering due to displacement scattering is found. Compared with the diffuse scattering of Ni-rich Ni-Au, the
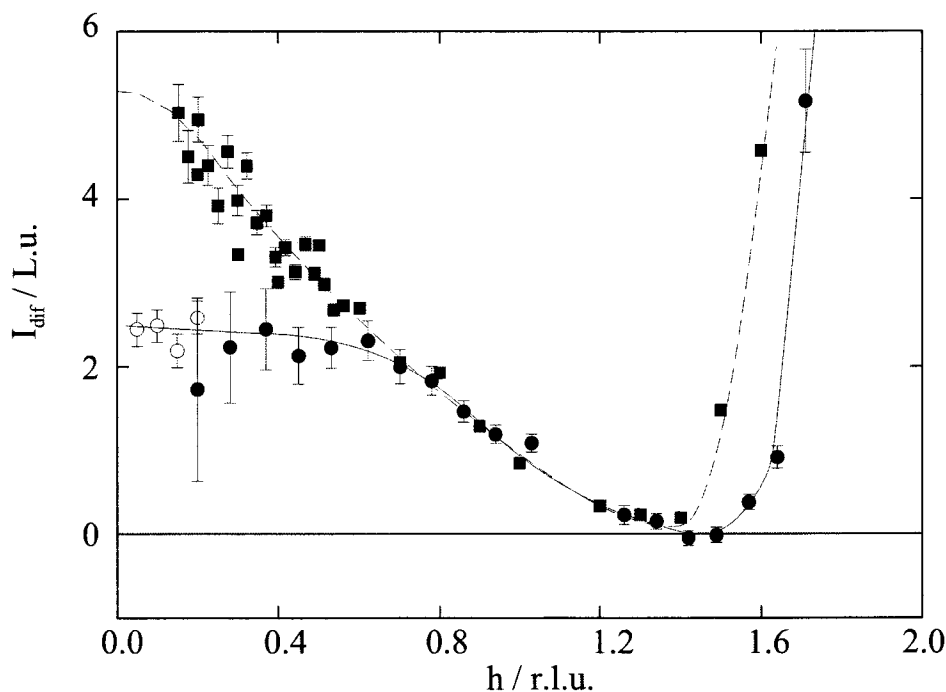
Fig. 22: Small-angle (o) and wide-angle scattering (•) intensities I_{dif} (in Laue units) of ^{58}Ni-60 at.% Au along h00. The wide-angle scattering of ^{58}Ni-8.4 at.% Au (■) is also shown. A dashed and a solid line serve as guide for the eyes.

position of the minimum is slightly shifted towards the 200 reflection, maybe just reflecting the different weighting of the species-dependent static atomic displacements in both alloys.

5 Discussion

A main result of the present study is that short-range decomposition and not short-range order is observed for [58]Ni-8.4 at.% Au above the miscibility gap. An increase in the elastic diffuse scattering towards 000 was demonstrated by means of elastic diffuse neutron scattering (see Fig. 23). In contrast to the X-ray results for [58]Ni-60 at.% Au [Wu83], no clear maxima along $h00$ were noticed. A short-range decomposed state above a miscibility gap is at variance with almost all diffuse X-ray scattering studies on Ni-Au alloys at temperature [Flin53], [Wu83] or of alloys quenched from the solid solution [Flin53]. The only exception is the conclusion in favor of decomposition from the evaluation of the short-range order scattering by Borie and Sparks of Ni-60 at.% Au data of Moss and Averbach (Fig. 7 in [Moss67]).

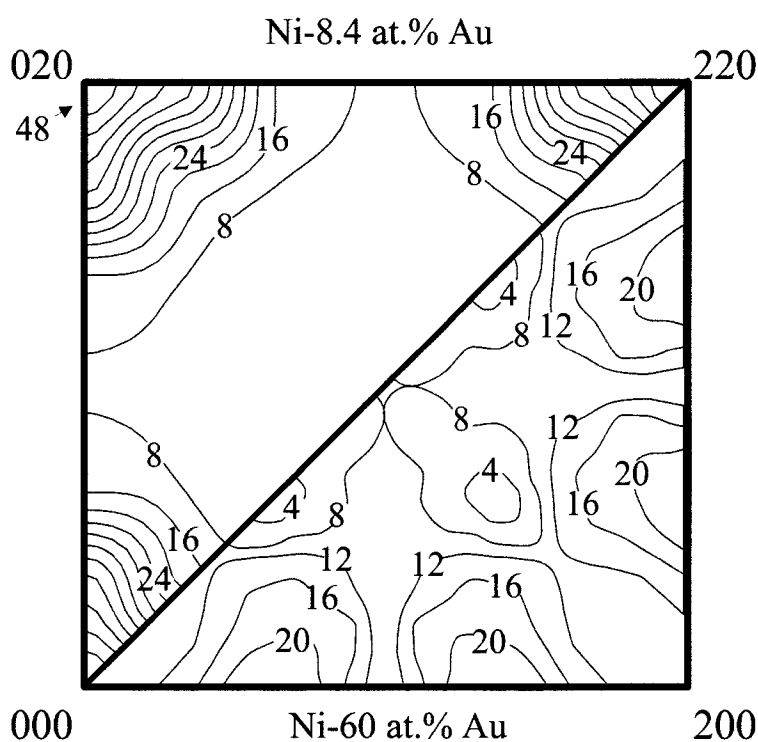The largest discrepancy between the short-range order scattering patterns of

Fig. 23: Short-range order scattering I_{SRO} (in 0.1 Laue units) from [58]Ni-8.4 at.% Au and from Ni-60 at.% Au [Wu83] at $h_1 h_2 0$ positions.

[58]Ni-8.4 at.% Au and Ni-60 at.% Au [Wu83] is noted for the region around 000 (see Fig. 23). This coincides with the extended range of 0.45 r.l. u. around the fundamental reflections where Wu and Cohen [Wu83] found it increasingly difficult to separate short-range order scattering from dynamic and static displacement scattering (as indicated by the large R value between the recalculated and as-measured diffuse scattering intensities). It is therefore not too surprising that the short-range order parameters of Wu and Cohen [Wu83] strongly differ from the present result, with $\alpha_{110} = 0.04(5)$ and $\alpha_{200} = 0.15(4)$. One might argue that the investigation at elevated temperature by Wu and Cohen[Wu83] was performed for an alloy with a much larger Au fraction and that diffuse scattering was never measured at sufficiently small angles. To provide experimental evidence for an increase in scattering intensity near the incident beam direction, the small-angle neutron scattering of a [58]Ni-60 at.% Au polycrystal (quenched sample) and the elastic diffuse neutron scattering of a [58]Ni-60 at.% Au single crystal were measured ($h00$ scan) at 1023 K. The calibrated scattering intensity along $h00$ (see Fig. 22) increases near the incoming beam, a feature that has to be attributed to short-range decomposition. The small-angle scattering and the elastic diffuse scattering smoothly merge. It is concluded that Ni-Au solid solutions above the miscibility gap are short-range decomposed.

The present results allow especially the following points to be addressed and commented.

(i) From electronic structure calculations [Wolv98], short-range order is expected for a broad range of compositions. The suggested directional dependence of the compositional modulations either along $\langle 100 \rangle$ (for Ni-60 at.% Au) or along $\langle 1\frac{1}{2}0 \rangle$ (for Ni-25 at.% Au) could not be investigated as no such modulations were observed at all. In contrast to the predictions of Wolverton and coworkers [Wolv98], no problems arise when determining the miscibility gap from the effective pair interaction parameters using Monte Carlo simulations, as there is a positive and not a negative value for the nearest-neighbor pair interaction parameter.

(ii) Asta and Foiles [Asta96] compared Ni-Au with two other alloy systems, Ni-Cu and Ag-Cu, that also show large miscibility gaps. Based on the energy of formation (see section 2.3) defined by de Fontaine and Cook [deFo79], Asta and Foiles [Asta96] used two approaches in their electronic structure calculations: effective pair interaction parameters with (i) chemical and constituent strain energy contributions (lattice relaxations owing to the different atomic sizes of the constituents) and (ii) only chemical contributions. For Ni-Cu

with a small size misfit of 2.5%, the nearest-neighbor parameter is negative in both cases, consistent with diffuse neutron scattering experiments on samples quenched from above the miscibility gap [Moze68], [Vrij78], [Wagn80]. For Ni-Au (and Ag-Cu), even a change in sign of the nearest-neighbor parameter is found between the two approaches; a negative sign corresponding to short-range decomposition is obtained if both chemical and constituent strain energy contributions are considered. Thus, only case (i) is consistent with the results presented in this work.

(iii) In bulk Ni-Au samples, a transient ordering phenomenon has been noted [Sanadze64], [Zhao99]. Sanadze and coworkers [Sanadze64] found the ordered phases Au_3Ni ($L1_2$), $AuNi$ ($L1_0$), and $AuNi_3$ ($L1_2$), using X-ray powder diffraction and resistivity measurements. For Ni-rich Ni-Au alloys aged at 800 to 1000 K, metastable $L1_2$ and $L1_0$ ordered states were found. Zhao and Notis [Zhao99] checked the experimental results of Sanadze and coworkers [Sanadze64] for Ni-50 at.% Au and Ni-60 at.% Au using transmission electron microscopy. Contrary to Sanadze and coworkers [Sanadze64], they only found superlattice reflections of the $L1_0$ superstructure in reversion experiments (long-term aging at 473 K and subsequent aging at 723 K). For Ni-8.4 at.% Au, neither the configurational analysis nor the effective pair-interaction parameters obtained from an inverse Monte-Carlo analysis gave hints for a metastable state with $L1_2$ structure. Enhancement factors larger than one found for the characteristic configurations of $L1_0$, indicate a plausible metastable state with $L1_0$ structure, consistent with the results of Zhao and Notis [Zhao99]. Still, the largest enhancement factor and abundance were found for small Au clusters consisting of a tetrahedron and an attached fifth Au atom.

The data correction and calibration used in this work were based on a reduction in the transmission factor at elevated temperatures observed for [58]Ni-8.4 at.% Au. A similar reduction of the transmission factor was also observed for Fe-20.6 at.% Al and [58]Ni-9.6 at.% Ti. This reduction was attributed to an increase in the thermal diffuse scattering, previously not considered in the linear absorption coefficient. Assuming that the thermal diffuse scattering cross-section is equivalent to the incoherent and coherent one-phonon scattering, the total thermal diffuse scattering cross-section was calculated according to Kothari and Singwi [Koth59]. Including this cross-section into the linear absorption coefficient and the transmission factor allowed the temperature dependence of the experimentally determined transmission factors to be calculated.

Thus, the thermal diffuse scattering was considered in the linear absorption coefficient μ, the transmission factor A and the correction for multiple scattering D. As for vanadium at room temperature a value for the transmission factor near 1 was calculated, no correction for vanadium was required. With this new procedure, a value of α_{000} near 1 was found for ^{58}Ni-8.4 at.% Au and Fe-21.9 at.% Al.

The quantitative description of the local atomic arrangement of ^{58}Ni-8.4 at.% Au based on a previously proposed correction for α_{000} developped from a diffuse scattering experiment performed on Fe-Al and subsequently used for ^{58}Ni-8.4 at.% Au [Port02] is in close agreement with the results presented in this work. In the correction used previously, half of the deviation in α_{000} from 1 was corrected by an additive term and half by a multiplicative factor. It is concluded that a correction for α_{000} of the elastic coherent scattering based solely on an additive term or a multiplicative factor is not correct. The evaluation procedure used in this work provides an explanation for the large variation in α_{000} found in diffuse neutron scattering by [Pier91], [Caud92] and [Boll97].

Whether the new procedure is also significant at room temperature, was also tested calculating the ratio of the transmission factors at room temperature and 0 K. For ^{58}Ni-8.4 at.% Au, Fe-21.9 at.% Al, ^{58}Ni-9.6 at.% Ti and ^{58}Ni-5.8 at.% Ti the ratios were found to deviate at most by 8% from one. Since the correction term of the multiple scattering, that also increases with increasing temperature, is in the denominator of the expression used in the calibration, the corrected values of α_{000} are within the experimental error of 5%. It is concluded that at room temperature, the thermal diffuse scattering does not have to be included explicitly in the linear absorption coefficient μ and the transmission factor A as the effect is negligibly small.

A large scattering contribution observed in the small-angle neutron scattering of Ni-Au at elevated temperatures, changing approximately proportional to temperature, was also interpreted in terms of thermal diffuse scattering, as the additional scattering contribution was approximately calculated as incoherent and coherent one-phonon scattering (calculated as in Ref. [Koth59]). In the small-angle neutron scattering of other (binary) alloy systems, thermal diffuse scattering is also present at elevated temperatures. One example is the small-angle neutron scattering of Ni-11.3 at.% Ti polycrystals [Komp01] measured on aging at 873 K. After initial variations, the background scattering contribution determined from Porod plots (see Fig. 15b in [Komp01], is $\Sigma_{\text{total}}/4\pi = 7.1(5) \times 10^{-2}$ cm^{-1} sr^{-1}. This value is just the sum of the calculated values of the elastic coherent $(1.62 \times 10^{-2}$ cm^{-1} sr$^{-1})$, the elas-

tic incoherent (3.01×10^{-2} cm^{-1} sr^{-1}) and the thermal diffuse (2.73×10^{-2} cm^{-1}sr^{-1}) scattering, leading to $\Sigma_{\text{total}}/4\pi = 7.4 \times 10^{-2}$ cm^{-1} sr^{-1}. It is therefore proposed that in Ni-11.3 at.% Ti thermal diffuse scattering can be determined following the same procedure as for Ni-Au.

6 Outlook

Species-dependent static atomic displacements of a Ni-rich Ni-Au solid solution at 1083 K. In the present work, diffuse neutron scattering was employed to determine the local atomic arrangement in Ni-8.4 at.% Au. In contrast to previous diffuse X-ray scattering investigations, a short-range decomposed (and not short-range ordered) state was found in the solid solution above the miscibility gap. The large species-dependent static atomic displacements due to the large difference in the atomic sizes, however, remained undetermined as only a compositionally weighted average of these displacements can be obtained from the neutron scattering of one particular alloy.

Species-dependent static atomic displacements are a prerequisite for a complete description of the microstructure of Ni-Au. They may then be compared with results of other approaches like those based on molecular dynamics simulations. Presently, the best way to get values of the species-dependent static atomic displacements is achieved using X-rays and varying deliberately the scattering contrast by tuning the incident wavelength close to the absorption edges of the constituents (referred to as 3λ-method). For neutrons, a variation in the scattering contrast can only be achieved by employing two alloys of identical microstructure, but different isotopic contents. Such a procedure has not yet been implemented for any binary alloy. Ni-Au is especially suited for isotopic replacement as the scattering length contrast $b_{Ni} - b_{Au}$ not only changes its value, but even its sign (from 6.8 fm when employing the Ni-58 isotope to -4.8 fm when employing the Ni-60 isotope). The largest problem is that the same microstructural state must be present in both alloys.

A simple rule to correlate the presence of short-range order or short-range decomposition in an A-B alloy with the A-B nearest neighbor distance has been suggested by Chakraborty [Chak95]; if the A-B nearest neighbor distance is larger than the arithmetic mean of the A-A and B-B distances, the alloy shows short-range decomposition (short-range order). This rule is fulfilled up to now for all measurements where the 3λ-method was employed. The species-dependent static atomic displacements determined are small (in the range of 10^{-2} to 10^{-4} lattice parameters).

No information, however, is available for alloys with a large difference in the atomic sizes (e.g. Ni-Au). These alloys are most difficult to be characterized, as the

product of displacements weighted with the scattering vector is assumed to be small in the data evaluation. Additionally, the constituents of these alloys are no longer close neighbors in the periodic table and investigations using the 3λ-method are not possible.

References

[Asta96] Asta, M. and Foiles, S. M. (1996) Embedded-atom-method effective-pair-interaction study of the structural and thermodynamic properties of Cu-Ni, Cu-Ag, and Au-Ni solid solutions. *Phys. Rev. B* **53**, 2389-2404.

[Berg66] Bergsma, J. and Van Dijk, C. (1966) Pyrolytic graphite as a second order neutron filter. *Nuclear Inst. and Meth.* **51**, 121-124.

[Boll97] Le Bolloc'h, D. (1997) Diffusion diffuse de neutrons, interactions interatomiques et diagramme de phase dans Pt-V. Comparison avec Ni-V. Ph.D. thesis, Université Rennes.

[Buch99a] Bucher, R., Schönfeld, B., Kostorz, G. and Zolliker, M. (1999) Short-range order in Ni-rich Ni-Ti studied by diffuse neutron scattering. *Phys. Status Solidi A* **175**, 527-536.

[Buch99b] Bucher, R. (1999) Lokale Atomanordnungen in Ni-Ti and Fe-Al bei hohen Temperaturen. Ph.D. thesis 12269, ETH Zürich.

[Chak95] Chakraborty, B. (1995) Static displacements and chemical correlation in alloys. *Europhys. Lett.* **30**, 531-536.

[Caud92] Caudron, R., Sarfati, M., Barrachin, M., Finel, A., Ducastelle, F. and Solal, F. (1992) In-situ diffuse scattering of neutrons in alloys and application to phase diagram determination. *J. Phys. I* **2**, 1145-1171.

[Clap66] Clapp, P. C. and Moss, S. C. (1966) Correlation functions of disordered binary alloys. I. *Phys. Rev.* **142**, 418-427.

[Clap71] Clapp, P. C. (1971) Atomic configurations in binary alloys. *Phys. Rev. B* **4**, 255-270.

[Cole70] Colella, R. and Batterman, B. W. (1970) X-ray determination of phonon dispersion in vanadium. *Phys. Rev. B* **1**, 3913-3921.

[Cook69] Cook, H. E. and de Fontaine, D. (1969) On the elastic free energy of solid solutions-I. Microscopic theory. *Acta Metall.* **17**, 915-924.

[Cowl50a] Cowley, J. M. (1950) An approximate theory of order in alloys. *Phys. Rev.* **77**, 669-675.

[deFo79] de Fontaine, D. (1979) Configurational thermodynamics of solid solutions. in *Solid State Physics* (edited by H. Ehrenreich, F. Seitz and D. Turnbull) New York: Academic, vol. **34**, pp. 73-274.

[Diet89] Dietrich, S. and Fenzl, W. (1989) Corrections in disordered crystals and diffuse scattering of X-ray and neutrons. *Phys. Rev.* **39**, 8873-8899.

[Flin51] Flinn, P. A. and Averbach, B. L. (1951) Atomic arrangement in gold-nickel solid solutions. *Phys. Rev.* **83**, 1070.

[Flin53] Flinn, P. A., Averbach, B. L. and Cohen, M. (1953) Local atomic arrangements in gold-nickel alloys. *Acta Metall.* **1**, 664-673.

[Gehl65] Gehlen, P. C. and Cohen, J. B. (1965) Computer simulation of the structure associated with local order in alloys. *Phys. Rev. A* **139**, 844-855.

[Geor77] Georgopoulos, P. and Cohen, J. B. (1977) The determination of short-range order and local atomic displacements in disordered binary solid solutions. *J. Phys. (Paris) Colloq.* **38**, C7, 191-196.

[Gero87] Gerold, V. and Kern, J. (1987) The determination of atomic interaction energies in solid solutions from short-range order coefficients - an inverse Monte-Carlo method. *Acta Metall.* **35**, 393-399.

[Hewa79] Hewat, A. W. (1979) Absorption corrections for neutron diffraction. *Acta Cryst. A* **35**, 248-250.

[Hofe82] Hofer, F. and Tokar, K. (1982) Thermodynamic properties of solid gold-nickel alloys. *Z. Phys. Chem.* **130**, 229-239.

[Hofe85] Hofer, F. and Warbichler, P. (1985) Spinodal decomposition in the gold-nickel system. *Z. Metallkd.* **76**, 11-15.

[Inde91] Inden, G. and Pitsch, W. (1991) Atomic ordering. in *Materials science and technology* (edited by R. W. Cahn, P. Haasen and E. J. Kramer) Weinheim: Wiley VCH, vol. **5**, pp. 497-552.

[Jian96] Jiang, X., Ice, G. E., Sparks, C. J., Robertson, L. and Zschack, P. (1996) Local atomic order and individual pair displacements of $Fe_{46.5}Ni_{53.5}$ and $Fe_{22.5}Ni_{77.5}$ from diffuse X-ray scattering studies. *Phys. Rev. B* **54**, 3211-3226.

[Kitt76] Kittel, C. (1976) Phonons II. Thermal properties. in *Solid state physics* Chichester: Whiley, pp. 146.

[Komp01] Kompatscher, M. (2001) Phase separation in Ni-rich Ni-Ti: the metastable states. Ph.D. thesis 14349, ETH Zürich.

[Koth59] Kothari, L. S. and Sigwi, K. S. (1959) Interaction of thermal neutrons. in *Solid state physics* (edited by H. Ehrenreich, F. Seitz and D. Turnbull) London: Academic Press, vol. **34**, pp. 109-190.

[Kriv69a] Krivoglaz, M. A. (1969) Diffuse scattering at concentration inhomogeneities in undistorted solutions. in *Theory of X-ray and thermal neutron scattering by real crystals* (edited by S. C. Moss) New York: Plenum, pp. 163-172.

[Kriv96b] Krivoglaz, M. A. (1996) Calculations of the Debye-Waller factor. in *X-ray and neutron diffraction in nonideal crystals* (edited by V. G. Baryakhtar, S. C. Moss, M. A. Ivanov and J. Peisl) Berlin: Springer, pp. 172-176.; Krivoglaz, M. A. (1996) Ideal solutions. in *X-ray and neutron diffraction in nonideal crystals* (edited by V. G. Baryakhtar, S. C. Moss, M. A. Ivanov and J. Peisl) Berlin: Springer, pp. 212-215.

[Kost96] Kostorz, G. (1996) X-ray and neutron scattering. in *Physical Metallurgy* (edited by R. W. Cahn and P. Haasen) Lausanne: North-Holland, 4th edition, p. 1116-99.

[Leib55] Leibfried, G. (1955) Gittertheorie der mechanischen und thermischen Eigenschaften der Kristalle. in *Handbuch der Physik: Kristallphysik I* (edited by S. Flügge) Berlin: Springer, vol. **7**, pp. 253.

[Loop66] Loopstra, B. O. (1966) Neutron powder diffractometry using a wavelength of 2.6 Å. *Nucl. Instr. and Methods* **44**, 181-187.

[Macg62] Macgillavry, C. H., Rieck, G. D., and Lonsdale, K. (1962) Physical and chemical tables. in *International tables for X-ray crystallography* (edited by C. H. Macgillavry, G. Rieck and K. Lonsdale), Birmingham: Kynoch Press, vol. **3**, pp. 264.

[Metr53] Metropolis, N., Rosenbluth, A. W., Rosenbluth, M. N., Teller, A. H. and Teller, E. (1953) Equation of state calculations by fast computing machines. *Chem. Phys.* **21**, 1087-1092.

[Moss67] Moss, S. C. and Averbach, L. B. (1967) Local atomic configurations in a gold-nickel alloy. in *Small-angle X-ray scattering* (edited by H. Brumberger) New York: Gordon and Breach, pp. 335-350.

[Moze68] Mozer, B., Keating, D. T. and Moss, S. C. (1968) Neutron measurement of clustering in the alloy CuNi. *Phys. Rev.* **175**, 868-876.

[Okam87] Okamoto, H. (1987) The Au-Ni (gold-nickel) system. in *Phase diagrams of binary gold alloys* (edited by H. Okamoto and T. B. Massalski) Materials Park, Ohio, ASM International, pp. 193-208.

[Pear58] Pearson, W. B. (1958) Cr-Ni. in *A Handbook of lattice spacings and structures of metals and alloys* , New York: Pergamon Press, pp. 552-553.; Pearson, W. B. (1958) Ni-V. in *A Handbook of lattice spacings and structures of metals and alloys*, New York: Pergamon Press, pp. 792-794.

[Pier91] Pierron-Bohnes, V., Cadvile, M. C., Finel, A. and Schaerpf, O. (1991) Influence of magnetism on chemical order in Fe-19.5 at.% Al single crystal. High temperature measurements of neutron diffuse scattering. *J. de Phys. I* **1**, 247-260.

[Port02] Portmann, M. J., Schönfeld, B., Kostorz, G. and Altorfer, F. (2002) Short-range order in Ni-8.4 at.% Au above the miscibility gap. *Phys. Rev. B* **65**, 024110, 1-7.

[Rein94] Reinhard, L. and Turchi, P. E. A. (1994) Transient ordered states in phase-separating alloys. *Phys. Rev. Lett.* **72**, 120-123.

[Rena95] Renaud, G., Belakhovsky, M., Lefebvre, S. and Bessière, M. (1995) Correlated chemical and positional fluctuations in the gold-nickel system: a synchrotron X-ray diffuse scattering study. *J. de Phys. III France* **5**, 1391-1405.

[Rous70] Rouse, K. D., Cooper, M. J. and Chakera, A. (1970) Absorption corrections for neutron diffraction. *Acta Cryst. A* **26**, 682-691.

[Sanadze64] Sanadze, V. V. and Gulyaev, G. V. (1964) Diffusion processes of crystalline phases in binary metallic systems. *Soviet Phys. - Cryst.* **8**, 695-700.

[Scho99a] Schönfeld, B. (1999) Local atomic arrangements in binary alloys. *Prog. Mater. Sci.* **44**, 435-543.

[Scho99b] Schönfeld, B., Portmann, M. J., Yu, S.-Y. and Kostorz, G. (1999) The type of order in Cu-10 at.% Au - evidence from diffuse scattering of X-rays. *Acta Mater.* **47**, 1413-1416.

[Schw87] Schwartz, L. H. and Cohen, J. B. (1987) Local ordering and clustering. in *Diffraction from Materials* (edited by B. Ilschner and N. J. Grant) Berlin: Springer, pp. 402-423.

[Sear75] Sears, V. F. (1975) Slow neutron multiple scattering. *Adv. Phys.* **24**, 1-45.

[Sear92] Sears, V. F. (1992) Neutron scattering lengths and cross sections. *Neutron News* **3**, 26-37.

[Seig52] Seigle, L. L., Cohen, M. and Averbach, B. L. (1952) Thermodynamic properties of solid nickel-gold alloys. *Trans. AIME* **194**, 1329-1337.

[Sell66] Sellars, C. M. and Maak, F. (1966) The thermodynamic properties of solid Au-Ni alloys at 775°C and 935°C. *Metall. Trans.* **236** 457-464.

[Simm71] Alers, G. A., Neighbours, J. R. and Sato, H. (1960) Temperature dependent magnetic contributions to the high field elastic constants of nickel and an Fe-Ni alloy. *Phys. Chem. Solids* **13**, 40-55.; Neighbours, J. R. and Alers, G. A. (1958) Elastic constants of silver and gold. *Phys. Rev.* **111**, 707-712.

[Spar66] Sparks, C. J. and Borie, B. (1959) Methods of analysis for diffuse X-ray scattering modulated by local order and atomic displacement. in *Local atomic arangements studied by X-ray diffraction* (edited by J. B. Cohen and J. E. Hilliard) New York: Met. Soc. Conf., Gordon and Breach, vol. **36**, pp. 5-50.; Borie, B. and Sparks, C. J. (1959) The interpretation of intensity distribution. *Acta Cryst. A* **27**, 198-202.

[Squi96] Squires, G. L. (1996) Neutron scattering - basic theory. in *Introduction in thermal neutron scattering.* New York: Mineola, Dover Publications, Inc., pp. 22.

[Tibb79] Tibballs, J. E. (1979) The role of Debye-Waller-factor measurement in the analysis of diffuse scattering data. *Acta Cryst. A* **35**, 61-62.

[Vill97] Villars, P. and Calvert, L. D. (1997) $Pd_{81}V_{19}$. in *Pearson's Handbook - Desk edition - Crystallographic data for intermetallic phases - CrSi-Zr*, Ohio: ASM International, Materials Park, pp. 2683.; Villars, P. and Calvert, L. D. (1997) Pt-V. in *Pearson's Handbook - Desk edition - Crystallographic data for*

intermetallic phases - CrSi-Zr, Ohio: ASM International, Materials Park, pp. 2716.

[Vine54] Vineyard, G. H. (1954) Multiple scattering of neutrons. *Phys. Rev.* **96**, 93-98.

[Vrij78] Vrijen, J. and Radelaar, S. (1978) Clustering in Cu-Ni: A diffuse neutron-scattering study. *Phys. Rev. B* **17**, 409-421.

[Wagn80] Wagner, W., Poerschke, R., Axmann, A. and Schwahn, D. (1980) Neutron-scattering studies of electron-irradiated ^{62}Ni-41.4 at.% ^{65}Cu alloys. *Phys. Rev. B* **21**, 3087-3099.

[Will72] Williams, O. R. (1972) A computer program for the reduction of diffuse x-ray data from solid solutions. Report ORNL-4828, Oak Ridge, Tennessee, pp. 1-33.

[Wolv97] Wolverton, C. and Zunger, A. (1997) Ni-Au: A testing ground for theories of phase stability. *Comput. Mater. Sci.* **8**, 107-121.

[Wolv98] Wolverton, C., Ozoliņš, V. and Zunger, A. (1998) First-principles theory of short-range order in size-mismatched metal alloys: Cu-Au, Cu-Ag, and Ni-Au. *Phys. Rev. B* **57**, 4332-4348.

[Wu83] Wu, T. B. and Cohen, J. B. (1983) Clustering in a Au-Ni alloy above the miscibiliy gap. *Acta Metall.* **31**, 1929-1935.

[Zhao99] Zhao, J.-C. and Notis, A. (1999) Ordering transformation and spinodal decomposition in Au-Ni alloys. *Metall. and Mater. Trans. A* **30**, 707-716.

Appendices

A Summary of α_{000} values from diffuse neutron scattering at elevated temperatures

In the following a summary of (elastic) diffuse neutron scattering experiments performed at elevated temperatures is presented (see Table 10). Most of the experiments were performed using a time-of-flight spectrometer and scattering intensities were determined in planes of reciprocal space. The elastic diffuse scattering experiments performed using a triple-axis spectrometer, were measured within a three-dimensional volume of reciprocal space. Both scattering techniques are time consuming, the time-of-flight technique due to reduced neutron flux in consequence of the chopping and the triple-axis technique due to the point-per-point measurement.

B Monte Carlo simulations

The expectation value $\langle A \rangle_{\text{eq}}$ of an observable A is given by

$$\langle A \rangle_{\text{eq}} = \frac{\sum_\tau A(\tau) e^{-H(\tau)/k_{\text{B}}T}}{\sum_\tau e^{-H(\tau)/k_{\text{B}}T}}, \tag{86}$$

i.e. the weighted average of A over all possible configurations τ. Since the number of configurations increases as $N!/(N_{\text{B}}!N_{\text{A}}!)$ for a canonical ensemble, the sum in eq. (86) can not be calculated explicitly. Therefore, configurations are taken into consideration according to the Boltzmann distribution (importance sampling according to Metropolis and coworkers [Metr53]). Then, the sum in eq. (86) is reduced to the arithmetic average of values obtained for the observable A in the sampling

$$\langle A \rangle_{\text{eq}} \cong \frac{1}{M} \sum_{\tau=1}^{M} A(\tau). \tag{87}$$

For the transition from an original configuration i to a new configuration j, the detailed balance is expressed by

$$W_{i \to j} e^{-H_i/k_{\text{B}}T} = W_{j \to i} e^{-H_j/k_{\text{B}}T} \tag{88}$$

where $W_{i \to j}$ is the transition probability. The condition of detailed balance implies that, at equilibrium, the average number of transitions $i \to j$ is the same as the

average number of inverse transitions $j \to i$. Only the ratio of $W_{i\to j}$ and $W_{j\to i}$ is univocally determined.

Table 10: Summary of the α_{000} values obtained from diffuse neutron scattering experiments at elevated temperatures. In addition, values of the linear absorption coefficients μ_{cal} (thermal diffuse scattering not included) and μ_{lit} found in literature are shown.

Authors	alloy	T [K]	α_{000}	μ_{cal} [cm^{-1}]	μ_{lit} [cm^{-1}]	technique
[Boll97]	Pt-33 at.% V	1488	0.62	1.14	1.12	TOF*
	Pt-20 at.% V	1032	0.94	1.14	1.10	TOF*
		1219	0.91	1.13	1.09	
		1419	0.99	1.13	1.09	
	Pt-11 at.% V	1224	0.85	1.09	1.08	TOF*
	Ni-11 at.% V	774	0.77	1.06	1.26	TOF**
[Caud92]	Pd-25 at.% V	1103	0.96	0.76	0.35	TOF*
	Ni-25 at.% V	1373	0.93	1.18	1.23	TOF**
	Ni-33 at.% V	1228	0.44	1.40	1.26	TOF**
		1248	0.45	1.40	1.26	
		1343	0.45	1.40	1.26	
		1413	0.47	1.39	1.26	
	Ni-25 at.% Cr	833	0.75	0.96	0.90	TOF**
		993	0.20	0.95	0.90	
	Ni-33 at.% Cr	923	0.87	0.93	0.86	TOF**
		1083	0.72	0.93	0.86	
[Pier91]	Fe-19.5 at.% Al	973	1.49			TOF
		1073	1.20			TOF
		1173	1.38			TOF
		1273	1.12			TOF
		1373	1.04			TOF
		1473	1.01			TOF
		1573	1.03			TOF
[Buch99a]	Fe-21.9 at.% Al	878	0.79			TAS
		966	0.69			TAS
		1073	0.48			TAS
[Buch99b]	[58]Ni-5.8 at.% Ti	293	0.97			TAS
	[58]Ni-9.6 at.% Ti	1103	0.60			TAS
[Port02]	[58]Ni-8.35 at.% Au	1083	0.59			TAS

*Lattice parameters found in [Vill97].
**Lattice parameters found in [Pear58].
TAS = triple-axis spectrometer, TOF = time-of-flight

In this work, $W_{i \to j}$ is expressed by

$$W_{i \to j} = \frac{e^{-\Delta H_{i \to j}/k_B T}}{1 + e^{-\Delta H_{i \to j}/k_B T}} \qquad (89)$$

where $\Delta H_{i \to j} = H_i - H_j$ is the energy difference of the configurations. Although one could determine $\langle A \rangle_{eq}$ after each sucessfull exchange of two atoms, averaging over a set of exchanges in the model crystal reduces correlation effects that could occur for subsequent exchanges.

Using Monte-Carlo simulations any state in thermal equilibrium can be described assuming:

(i) The ordering energy and the effective pair interaction parameters are temperature independent. If the character of the pair interaction parameters changes (e.g., at the onset of ferromagnetism below the Curie temperature), the ordering energy also changes.

(ii) As the character of the pair interactions changes as the number of valence electrons changes the effective pair interaction parameters are composition dependent. The variations are small, if binary alloys with not too different compositions are compared (see, e.g., Cu-Au [Scho99b]).

C   Inverse Monte Carlo method

Whereas in Monte Carlo simulations (see appendix B) the $\alpha_{d\underline{r}}$ are calculated for a given set of effective pair interaction parameters, the inverse Monte Carlo method introduced by Gerold and Kern [Gero87] allows the effective pair interaction parameter to be determined for a given set of $\alpha_{d\underline{r}}$. Provided that the $\alpha_{d\underline{r}}$ represent a state in thermal equilibrium, these $\alpha_{d\underline{r}}$ correspond to the thermal average $A_0 = \langle A \rangle_{eq}$ given by (86). Under these conditions, the weighted average over the deviations $\Delta A_{0 \to i}$ due to thermal fluctuations i from the thermal average has to be zero

$$\sum_i W_{0 \to i} \Delta A_{0 \to i} \cong 0. \qquad (90)$$

Similar to the Monte Carlo simulation, the transition probabilities $W_{0 \to i}$ are given by the condition of the detailed balance in eq. (88) and are set to

$$W_{0 \to i} = \frac{e^{-\Delta H_{0 \to i}/k_B T}}{1 + e^{-\Delta H_{0 \to i}/k_B T}}. \qquad (91)$$

The corresponding energy change is

$$\Delta H_{0\to i} = 2 \sum_{d\underline{r}} \Delta N_{i,d\underline{r}}^{\mathrm{BB}} V_{d\underline{r}} \tag{92}$$

using the ordering energy defined in eq. (59) and the short-range order parameters defined in eq. (5). The variable $\Delta N_{i,d\underline{r}}^{\mathrm{BB}} = N_0^{\mathrm{BB}} - N_i^{\mathrm{BB}}$ is the change in the number of BB pairs at a distance $d\underline{r}$, when a virtual exchange is considered.

Inserting $\Delta N_{i,d\underline{r}}^{\mathrm{BB}}$ as observable $\Delta A_{0\to i}$ in eq. (90), one obtains nonlinear equations

$$\sum_i \Delta N_{i,d\underline{r}}^{\mathrm{BB}} \frac{e^{-2\sum_{d\underline{r}} \Delta N_{i,d\underline{r}}^{\mathrm{BB}} V_{d\underline{r}}/k_{\mathrm{B}}T}}{1 + e^{-2\sum_{d\underline{r}} \Delta N_{i,d\underline{r}}^{\mathrm{BB}} V_{d\underline{r}}/k_{\mathrm{B}}T}} = 0 \tag{93}$$

for each neighboring shell $d\underline{r}$. The effective pair interaction parameters $V_{d\underline{r}}$ represent the numerical solution of the corresponding system of coupled equations.

D Coherent and incoherent scattering cross-sections of pure metals and binary alloys

In Table 11, the scattering lengths of the atoms used in this work are summarized. Vanadium and nickel show large incoherent scattering cross-sections. While the incoherent scattering of vanadium is due to the nuclear spin of the $^{51}\mathrm{V}$ isotope, the incoherent scattering of nickel is mainly due to the isotopic contents.

The elastic coherent scattering cross-section of a binary alloy A-B is given by

$$\sigma_{\mathrm{coh}} = 4\pi c_{\mathrm{A}} c_{\mathrm{B}} |b_{\mathrm{A}} - b_{\mathrm{B}}|^2 \tag{94}$$

where c_i is the concentration and b_i the coherent neutron scattering length of the component i. The elastic incoherent scattering cross-section is expressed by

$$\sigma_{\mathrm{inc}} = c_{\mathrm{A}} \sigma_{\mathrm{inc,A}} + c_{\mathrm{B}} \sigma_{\mathrm{inc,B}} \tag{95}$$

where $\sigma_{\mathrm{inc,i}}$ is the incoherent scattering cross-section of the component i. The absorption scattering cross-section is given by

$$\sigma_{\mathrm{abs}} = [c_{\mathrm{A}} \sigma_{\mathrm{abs,A}} + c_{\mathrm{B}} \sigma_{\mathrm{abs,B}}] \frac{\lambda}{1.798\text{Å}} \tag{96}$$

where $\sigma_{\mathrm{abs,i}}$ is the absorption scattering cross-section of the component i.

Table 11: Values of b_{coh}, b_{inc} and σ_{abs} as well as the atomic number Z, the mass number A, the nuclear spin I and relative abundance c of the nuclides in the natural occurring elements V, Ni and Au taken from [Sear92].

Element	Z	A	I	c [%]	b_{coh} $[10^{-15}\mathrm{m}]$	σ_{inc} $[10^{-28}\mathrm{m}]$	$\sigma_{\mathrm{abs}}^{*}$ $[10^{-28}\mathrm{m}]$
V	23				-0.3824(12)	5.08(6)	5.08(4)
		50	6	0.25	7.6(6)	0.5(5) E	60.0(400)
		51	7/2	99.75	-0.402(2)	5.07(6)	4.9(1)
Ni	28				10.3(1)	13.3(3)	4.49(16)
		58	0	68.27	14.4(1)	0	4.6(3)
		60	0	26.10	2.8(1)	0	2.9(16)
		61	3/2	1.13	7.60(6)	1.9(3)	2.5(8)
		62	0	3.59	-8.7(2)	0	14.5(3)
		64	0	0.91	-0.37(7)	0	1.52(3)
Au	79		3/2		7.63(6)	0.43(5)	98.65(9)

*For $\lambda = 1.798\text{Å}$.
E: Estimated values for isotopes with low abundance.

E Least-squares fitting method

According to Williams [Will72] the p-dimensional linear equation system to solve is given by

$$I_i = \sum_{j=1}^{q} A_{ij} X_j \tag{97}$$

where I_i is a p-dimensional vector that contains the corrected scattering intensities of each position weighted with the square-root of the statistical error bar w_{hkl}. A_{ij} is a $p \times q$ coefficient matrix and X_j is the q-dimensional solution vector that contains a set of short-range order parameters α_{lmn}, linear displacement parameters γ_{lmn}^x and the quadratic displacement parameters δ_{lmn}^x and ϵ_{lmn}^{xy}. Therefore $\underline{X}$ and $\underline{I}$ are given by

$$\underline{X} = (\alpha_{000}, ..., \alpha_{lmn}, \gamma_{110}^x, ..., \gamma_{l'm'n'}^x, \delta_{000}^x, ..., \delta_{l''m''n''}^x, \epsilon_{110}^{xy}, ..., \epsilon_{l'''m'''n'''}^{xy}) \tag{98}$$

$$\underline{I} = (w_{000}^{1/2} I_{\mathrm{dif}}(000), ..., w_{hkl}^{1/2} I_{\mathrm{dif}}(hkl)). \tag{99}$$

By minimizing

$$\sum_{i=1}^{p} |I_i - \sum_{j=1}^{q} A_{ij} X_j^0| = \text{minimal},\qquad(100)$$

an estimate of the form

$$X_j^0 = \sum_{i=1}^{p} \left[\left(\underline{\underline{A}}^{\mathrm{T}} \underline{\underline{A}} \right)^{-1} \underline{\underline{A}}^{\mathrm{T}} \right]_{ij} I_i \qquad(101)$$

can be found, where $\underline{\underline{A}}^{\mathrm{T}}$ is the transposed matrix of $\underline{\underline{A}}$. The value of χ^2 is

$$\chi^2 = \frac{\sum_{i=1}^{p} \left(I_i - \sum_{j=1}^{q} A_{ij} X_j^0 \right)^2}{p - q} \qquad(102)$$

and therefore the standard deviation ΔX_i^0 of each parameter is given by

$$\Delta X_i^0 = \sqrt{\chi^2 \left(\underline{\underline{A}}^T \underline{\underline{A}} \right)^{-1}}.\qquad(103)$$

The quality of each fit with a variable number of parameters is given by χ^2, and the weighted R value is expressed by

$$R = \sqrt{\frac{\sum_{i=1}^{p} (I_i - \sum_{j=1}^{q} A_{ij} X_j^0)^2}{\sum_{i=1}^{p} I_i^2}}.\qquad(104)$$

Curriculum vitae

February, 1973	Born in Davos-Platz, Switzerland
1979 − 1985	Elementary school in Davos-Platz, Switzerland
1985 − 1992	Lateingymnasium at the Schweizerische Alpine Mittelschule Davos, Switzerland
1992 − 1993	Member of the Swiss cross country ski junior national team
1993 − 1998	Studies in physics at the ETH Zurich, Switzerland
1998	Diploma thesis at the ETH Zurich, Switzerland at the Institute of Applied Physics of Prof. Dr. G. Kostorz "Ordnung in Cu-10 at.% Au "
1998 − 1999	Member of the research staff at the R & D Center, ABB, Dättwil, Switzerland in the group of Dr. W. Paul
since April 1999	PhD in Physics at the ETH Zurich, Switzerland at the Institute of Applied Physics of Prof. Dr. G. Kostorz
since August 2000	Husband of Karin
since August 2001	Father of Silvana